Physics of the Earth and Planetary Interiors 216 (2013) 32–58

Contents lists available at SciVerse ScienceDirect

Physics of the Earth and Planetary Interiors

journal homepage: www.elsevier.com/locate/pepi

Thermal and compositional evolution of the martian mantle: Effects of phase transitions and melting

Thomas Ruedas[a,*], Paul J. Tackley[b], Sean C. Solomon[a]

[a] Department of Terrestrial Magnetism, Carnegie Institution of Washington, 5241 Broad Branch Road, NW, Washington, DC 20015, USA
[b] Institute of Geophysics, ETH Zürich, NO H9.1, Sonneggstrasse 5, 8092 Zürich, Switzerland

ARTICLE INFO

Article history:
Received 8 March 2012
Received in revised form 16 November 2012
Accepted 18 December 2012
Available online 28 December 2012
Edited by Mark Jellinek

Keywords:
Mars
Mantle convection
Phase transition
Thermoelastic properties
Melting

ABSTRACT

We present new numerical models for the thermochemical evolution of the mantle of Mars over the past 4 Gy. Specifically, we have developed a parameterized model of composition and thermoelastic properties of mantle material and combined it with a two-dimensional, anelastic, compressible convection and melting algorithm in a spherical annulus geometry; these models include a detailed treatment of the effects of solid–solid phase transitions and of compositional changes that accompany generation and removal of mantle partial melt during magmatism. Among other questions, we examine if a perovskite + ferropericlase layer (pv + fp) exists at the base of the martian mantle, if long-lived plumes can explain the volcanic provinces, under which circumstances Mars may still be volcanically active, and how iron- and radionuclide-rich Mars is. Results of the models are compared with geophysical and chemical observations from spacecraft and information from martian meteorites. Most models yield crustal thicknesses between ~75 and 90 km, ancient depths for the Curie temperatures of possible magnetic carriers that include the entire crust, and mechanical lithosphere thicknesses that increased from less than 100 km in the Noachian to 200–250 km now. Generally, models with a large core, Mg# = 0.75, and radionuclide contents derived from those suggested by Wänke and Dreibus (Chemistry and accretion history of Mars. Philos. Trans. R. Soc. Lond. A 349, 285–293, 1994) tend to explain observations best, but none of the models reproduces the full range of concentrations found in martian meteorites, thus implicitly supporting the idea that ancient chemical heterogeneities survive in the mantle. Only a subset of the models develops a pattern of mantle convection that evolves towards two or three large, long-lived plumes, and it takes at least ~2 Gy before this stage is reached, whereas models with a larger number of plumes or with plumes that are less stationary are more common. As Tharsis and probably Elysium are older than 2.5–3 Gy, either model assumptions more complex than those made in this study or a dynamical mode different from low-degree convection with long-lived large plumes is required to explain these major volcanic provinces. The effect of the mid-mantle phase transitions on mantle dynamics is rather weak, so that whole-mantle convection prevails; however, a basal pv + fp layer would form a dynamically separate unit and decouple the mantle and core to some extent.

1. Introduction

Mars, like Earth, is known to have differentiated into a metallic core and a silicate mantle, but important aspects of its internal structure remain uncertain. For instance, in the absence of seismological information, the radius of its core is known only to within several hundred kilometers from the planet's mass and moment of inertia and cosmochemical constraints (cf. Khan and Connolly, 2008, and references therein). The corresponding range of mantle thicknesses allows for the existence of a thin layer of $(Mg,Fe)SiO_3$ perovskite (pv) and ferropericlase (fp) at its base, at least during some periods in martian history. In contrast to the situation for Earth, the lithosphere of Mars consists of a single global plate, and the crust displays an ancient north–south dichotomy in thickness. Two large, long-lived volcanic provinces, Tharsis and Elysium, indicate a more localized pattern and isolated style of magmatism than on Earth. Because Mars is smaller than Earth, the gravitational acceleration g is smaller at the surface and is not approximately constant with depth as within Earth's mantle but decreases by about 20% from the surface to the core–mantle boundary (CMB). This decrease reinforces the diminution of buoyancy in the deeper parts of the mantle caused by a decrease in the volumetric thermal expansion coefficient α with depth, (e.g., Sohl and Spohn, 1997), reduces buoyancy effects in flow across phase boundaries, and renders more difficult the formation of strong, long-lived plumes at

---

* Corresponding author. Tel.: +1 202 478 8846; fax: +1 202 478 8821.
E-mail address: ruedas@dtm.ciw.edu (T. Ruedas).

0031-9201/$ - see front matter © 2012 Elsevier B.V. All rights reserved.
http://dx.doi.org/10.1016/j.pepi.2012.12.002

the CMB. All these characteristics indicate that the martian mantle experienced a thermal and compositional evolution quite different from that of Earth. In this paper we simulate this evolution over the past 4 Gy in an attempt to integrate several features and properties of the planet inferred from observations with a dynamical model of its interior.

In most geochemical models of Mars, the mantle has a bulk molar Mg/(Mg + Fe), or Mg#, of 0.75–0.8, (e.g., Wänke and Dreibus, 1994; Lodders and Fegley, 1997; Sanloup et al., 1999), markedly lower than the terrestrial value of $\sim$0.9, although values higher than 0.8 (Musselwhite et al., 2006) and lower than 0.75 (e.g., Sanloup et al., 1999) have also been postulated. Taking into account the difference between the polar and average moments of inertia, Sohl et al. (2005) considered the Mg# to lie at or somewhat higher than the upper end of the above range, whereas Khan and Connolly (2008) favored values at or near the lower end of that range on the basis of a joint inversion of several quantities. Because of the lower Mg#, the succession and structure of phase transitions in $(Mg,Fe)_2SiO_4$ within Mars will be somewhat different from those in Earth (Fig. 1). In particular, there is a regime where ringwoodite (rw, or γ phase) is stable in coexistence with olivine (ol, or α) at lower pressure than the stability region of wadsleyite (wd, or β). Moreover, the $\beta + \gamma$ two-phase loop covers a larger pressure interval than it would in a terrestrial composition, whereas the $\alpha + \beta$ loop and the stability field of pure wadsleyite are rather narrower in pressure or, in cold mantle, absent. The rw–(pv + fp) transition (if present) is slightly broader and occurs at slightly lower pressure; in cold mantle, there may be a narrow depth interval where ringwoodite coexists with ferropericlase and stishovite (st).

To avoid confusion with terrestrial nomenclature, we refer to the upper mantle downward to the top of the mid-mantle $(Mg,Fe)_2SiO_4$ transitions as the "upper layer" and to the underlying portion downward to the appearance of the perovskite phase as the "lower layer." For sufficiently small core radius, the latter may be separated from the core by a "basal layer" of pv + fp. Pressure increases more slowly with depth than in Earth, so the stability field of a given mineral phase or two-phase loop as defined by pressure covers a broader depth range. As a consequence, ringwoodite, which makes up only a small part of Earth's mantle, is a major constituent of the martian mantle.

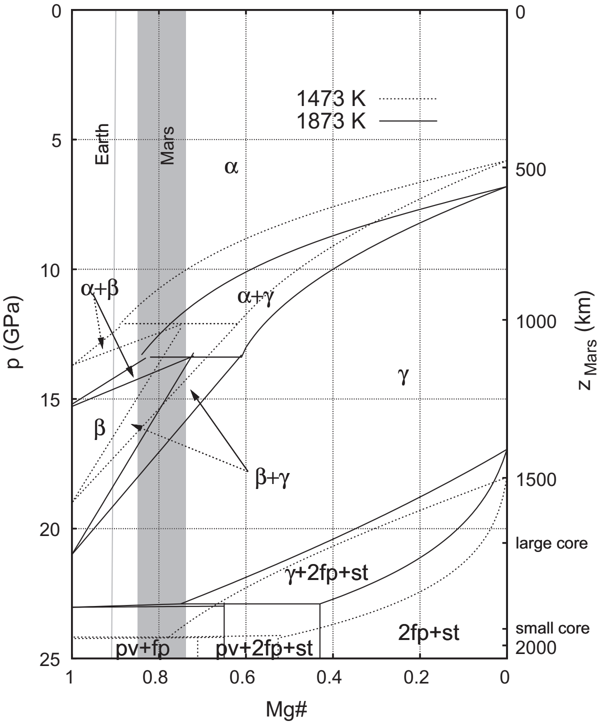

Fig. 1. Isothermal phase stability fields of $(Mg,Fe)_2SiO_4$ at two different temperatures versus pressure and Mg#. The depth scale z_{Mars} corresponds to the martian mantle and is approximately valid within the "Mars" interval (shaded) of Mg#. The names of mineral phases are abbreviated as follows: α – olivine, β – wadsleyite, γ – ringwoodite, pv – perovskite, fp – ferropericlase, st – stishovite.

The effects of the phase transitions of $(Mg,Fe)_2SiO_4$ on convection in the martian mantle with and without a perovskite layer have been studied extensively (e.g., Weinstein, 1995; Harder and Christensen, 1996; Breuer et al., 1997; van Thienen et al., 2006), in part to reconcile flow patterns with the temporal and spatial distribution of volcanism, particularly the existence of Tharsis and Elysium. Models with and without a perovskite layer have been able to reproduce such an upwelling pattern in some form. In some models (Breuer et al., 1997; van Thienen et al., 2006), mantle convection is more or less layered, which limits the applicability of parameterized modeling approaches. van Thienen et al. (2006), who also considered phase-related details of the mantle's viscosity structure and the effect of a hemispheric dichotomy in crustal thickness, argued that the dichotomy together with early cold downwellings can result in a small number of long-lived volcanic centers, a conclusion also supported by laboratory experiments (Wenzel et al., 2004). All these studies, however, utilized simplifications with regard to the phase diagram or other properties of mantle material. Most neglected transitions in phases other than $(Mg,Fe)_2SiO_4$ and treated that system in a simplified manner, e.g., by neglecting some transitions (Weinstein, 1995), fixing transitions at a given depth (Harder and Christensen, 1996), or using a terrestrial rather than a martian phase transition pattern (Breuer et al., 1997). The only full fluid dynamical convection studies so far that did consider the impact of Mg# on the pattern of phase boundaries were our own preliminary investigations, (e.g., Ruedas and Tackley, 2008) and a recent investigation by Michel and Forni (2011), although the latter did not include transitions in phases other than $(Mg,Fe)_2SiO_4$.

Melting and its impact on internal heating through the redistribution of radionuclides have received less attention for Mars in full fluid dynamic convection models, although it has been a common feature in parameterized evolution models. In fluid dynamic models, melting has often been neglected, and internal heating is typically included only as a constant term in the temperature equation. The density effect of depletion was studied by Schott et al. (2001) in a Cartesian geometry with a thermal conductivity that depended on pressure p and temperature T. They found that the thick, low-density depleted layer inhibits whole-mantle convection, but that the non-linear nature of thermal conductivity may stabilize long-lived plumes. Their model apparently did not include mineral phase transitions and neglected the redistribution of radionuclides due to melting. Kiefer (2003) and Li and Kiefer (2007) addressed melting and the redistribution of internal heat sources and concluded that convection should still be at least moderately vigorous if Mars is still magmatically active, as suggested by recent spacecraft observations; that the general convection pattern has remained stable over the history of the planet; and that about half the radionuclides still remain in the mantle if the abundances of Wänke and Dreibus (1994) are assumed. Drawbacks of those two studies, however, are that they imposed radionuclide partitioning between crust and mantle rather than relating it physically to melting, and that they did not consider phase boundaries. More recently, Ogawa and Yanagisawa (2011) calculated two-dimensional models that include internal heating and treat melting as a two-phase flow problem, whereby the heat sources are redistributed according to their partition coefficient. They proposed that the present state of Mars is the result of a "relaxation process" of a compositionally and stably layered early magma ocean on which a crust was built that incorporated an increasing fraction of heat-producing elements, especially as a result of plume magmatism. Similar to Schott et al. (2001), they used a Cartesian geometry instead of a spherical and they neglected phase transitions of $(Mg,Fe)_2SiO_4$, especially the possible presence of a basal pv + fp layer, as well as the substantial decrease of αg with depth.

Most similar to this work in methodology and its inclusion of detailed material characteristics is the recent study by Keller and Tackley (2009), who took mineral properties, phase transitions, and melting into account in three-dimensional spherical models of the first billion years of martian history. With a pronounced viscosity layering in a mantle without a basal layer, they found a convection pattern that consists of one planetary-scale rift-like upwelling and smaller-scale convection in the upper layer. Their models were also able to produce a crustal thickness pattern that resembles, to first order, the hemispheric dichotomy.

In this paper, we examine if a setup that incorporates a wide range of information on the thermochemical and transport properties of assumed martian mantle material but uses initial and boundary conditions as simple as those applied in most earlier convection studies (e.g., Weinstein, 1995; Harder and Christensen, 1996; Breuer et al., 1997; Kiefer, 2003) or implicit in one-dimensional parameterized models is able to reproduce a range of observations, including major structures such as the volcanic provinces. Of particular interest are the following questions: Is the core small enough to allow the existence of a (pv + fp) basal layer? Can the existence of Tharsis and Elysium be explained by long-lived plumes, and is Mars still volcanically active today? What are the Mg# of the martian mantle and the radionuclide contents of the mantle and crust? In order to address these questions, we combine a detailed model of composition and thermoelastic properties with the compressible convection algorithm implemented by Tackley (2008). Like Keller and Tackley (2009), we attempt to avoid many of the simplifications made in previous studies by integrating an even more thorough thermoelastic, petrological, and melting model into a convection algorithm that solves the anelastic, compressible dynamical equations instead of applying the Boussinesq or an extended Boussinesq approximation. We also account for the changes with depth of quantities such as g and α, which were neglected in some previous work (e.g., Harder and Christensen, 1996; van Thienen et al., 2006), address some of the effects of melting, e.g., on Mg# and radionuclides, and represent the core via a parameterized evolution model. The inclusion of a large amount of information about material properties may at first glance be perceived as the introduction of a large number of free parameters. We argue instead that we are limiting the number of free parameters by constraining them as well as possible with available empirical information and placing them into a physical context that strives to be internally consistent. Models in which chosen property values are known to be poor approximations and diminish the internal physical consistency of the model arguably have much more the character of free parameters than ours, even though they are usually not regarded as such.

Models that make simplifying assumptions for understanding fundamental physical processes in idealized systems and for providing guidance in the interpretation of observations are certainly valuable. However, simple models tend to target a specific problem and have difficulties reproducing a broad range of different observations made in a real planet. Our goal in this study is not to establish fundamental physical relations but to take first steps towards explaining the full spectrum of available observations of a complex planetary body. To this end, we must strive to reproduce the parts of a planet's complexity that are reasonably well constrained and leave as degrees of freedom those parts that are not. The level of detail implemented in our models allows us to compare the model results with a range of geophysical and geochemical observations and inferences from independent studies that is much wider than in previous work; the purpose of our study apart from its application to Mars is therefore to showcase the possibilities of geodynamical modeling as a tool for prediction and interpretation. We compare the predictions of our models, which cover the last 4 Gy, for almost a dozen geophysical and geochemical observables – crustal and lithospheric thickness, heat flow, geoid, moment of inertia, depth to the Curie temperature, volcanic activity patterns, and radionuclide abundances – with published models and observations; even more observables, in particular seismic velocities and electrical conductivity, could also be predicted but have been omitted because no observational constraints are available at this point, although the Interior Exploration using Seismic Investigations, Geodesy and Heat Transport (InSight) mission (e.g., Banerdt et al., 2012) that is to fly to Mars in 2016 will partly alleviate the scarcity of data. We evaluate the success of models without addressing the question of water in the martian mantle and its effects on rheology and melting, a topic we address in a companion paper (Ruedas et al., submitted for publication).

2. Method

In this section, we give an outline of the methods to calculate various properties of mantle material, which are at the focus of this paper. The calculation of the properties of the core used in the parameterized core model that provides the boundary condition at the CMB is described in Appendix B.

2.1. Thermoelastic properties and thermal conductivity

The calculation of thermoelastic properties must take into account the p and T dependence of α, the isothermal bulk modulus K_T, and the isobaric heat capacity c_p. We chose an approach based on expressions parameterized in T at zero pressure:

$$\alpha(0,T) = a_0 + a_1 T + \frac{a_2}{T} + \frac{a_3}{T^2} \tag{1}$$

$$K_T(0,T) = \left(b_0 + b_1 T + b_2 T^2 + b_3 T^3\right)^{-1} \tag{2}$$

$$c_p(0,T) = c_0 + c_1 T + \frac{c_2}{T^2} + c_3 T^2 + \frac{c_4}{T^3} + \frac{c_5}{T} + \frac{c_6}{\sqrt{T}} \tag{3}$$

for constants a_i, b_i, and c_i, and the temperature T in K (Saxena et al., 1993); the procedure outlined in the following does not depend on the specific form. The isothermal bulk modulus was taken to be linear in p, and its pressure derivative to be linear in T:

$$K_T(p,T) = K_T(0,T) + \left[K'_{T0} + \frac{\mathrm{d}K'_{T0}}{\mathrm{d}T}(T - T_0)\right]p. \tag{4}$$

In the following, we denote the term in brackets by K'_T. The values for a_i, b_i, and c_i as well as for the molar volume at standard conditions, V_0, the pressure derivative of K_T at zero pressure, K'_{T0}, and its temperature derivative, $\mathrm{d}K'_{T0}/\mathrm{d}T$ were taken from the self-consistent thermochemical database for mineral end-members compiled by Saxena et al. (1993).

The computation consisted of two steps. The first step was isobaric heating to the target temperature T at surface pressure by using Eqs. (1)–(3) and determining the molar volume at standard pressure by analytical integration of Eq. 1:

$$V(0,T) = V_0 \exp\left(\int_{T_0}^{T} \alpha(T')\mathrm{d}T'\right) = V_0 \exp\left[a_0(T - T_0) + \frac{a_1}{2}(T^2 - T_0^2) + a_2 \ln\frac{T}{T_0} - a_3\left(\frac{1}{T} - \frac{1}{T_0}\right)\right]. \tag{5}$$

The second step was isothermal compression to the target pressure using p-dependent expressions for α, K_T, and c_p, whereby certain relations among these parameters are maintained. Specifically, we applied the relation

$$\left(\frac{\partial \alpha}{\partial p}\right)_T = \frac{1}{K_T^2}\left(\frac{\partial K_T}{\partial T}\right)_p \tag{6}$$

and Eq. 4 to integrate α to pressure p. To integrate c_p from 0 to a pressure p in a similar way, we used the relation

$$\left(\frac{\partial c_p}{\partial p}\right)_T = -VT\left[\alpha^2 + \left(\frac{\partial \alpha}{\partial T}\right)_p\right] \tag{7}$$

(e.g., Pankov et al., 1998) with the temperature derivative determined from the $\alpha(p, T)$ calculated before. Except for the integration of $(\partial c_p/\partial p)_T$, all calculations can be done in closed form, although this may not be the most convenient form for practical purposes.

After having computed the properties of the end-members for any p and T in this manner, we determined the properties of the bulk material by combining end-members to form (ideal) solid solutions. The density of each was calculated from the mole-weighted average of the end-member molecular masses, m_{ss}, and molar volumes, V_{ss}. For the thermal expansion coefficient, the expression for the solid-solution molar volume can be substituted into the definition of α, yielding:

$$\alpha_{ss} = \frac{1}{\sum \underline{X}_i V_i}\left(\frac{\partial}{\partial T}\right)_p \left(\sum \underline{X}_i V_i\right) = \frac{\sum \underline{X}_i V_i \alpha_i}{V_{ss}}, \tag{8}$$

where $\underline{X}_i$ is the molar fraction of the ith component of the solid solution (e.g., Ita and Stixrude, 1992). The expansion coefficient of the mineral composite follows from the bulk density and the volume fractions, expansion coefficients, and densities of the constituent solid solutions by a similar calculation (e.g., Sohl and Spohn, 1997). The composite heat capacity was determined as a weighted sum according to molar or weight fraction.

Thermal conductivity k, which is tied to some extent to the thermoelastic properties, was also calculated in two steps. k and the thermal diffusivity $\kappa = k/(\varrho c_p)$ were determined for each mineral phase individually using the data of Hofmeister et al. (2007) for the phonon contribution and adding the (relatively unimportant) pressure-independent radiative component as given by Hofmeister (1999). The pressure dependence of the phononic part of k and κ is not well constrained experimentally and was assumed here to scale with the bulk modulus (Hofmeister et al., 2007). The conductivity of the bulk material was taken to be the mean of the generalized Hashin–Shtrikman bounds for a composite of the individual minerals (Berryman, 1995).

The surface of the planet is not solid, compact material but is porous and cracked as a consequence of eons of meteorite impacting and other weathering processes. As in Earth, overburden pressure closes the voids at depth, and this closure can be modeled with an exponential function. The spatial variation in k potentially has considerable influence on the thermal evolution of a planet (Schumacher and Breuer, 2006; Schumacher and Breuer, 2007). We assumed that the material properties for which modification by porosity affects dynamics most directly are density and thermal conductivity, both of which would be substantially reduced near the surface. From work by Head and Wilson (1992), Leone et al. (2011) derived the pressure-dependent formulae

$$\varrho(p) = \varrho_{\text{solid}}(1 - \varphi), \tag{9a}$$

$$k(p) = k_{\text{solid}}(1 - 1.738\varphi + 0.8228\varphi^2), \tag{9b}$$

where $\varphi = \varphi_{\text{surf}} \exp(-11.8p)$ is the porosity, ϱ_{solid} and k_{solid} are the density and thermal conductivity of the compact solid material, respectively, and the pressure p is in GPa. The porosity function approaches zero within approximately 30 km depth on Mars, which corresponds to the uppermost two grid rows in our models.

2.2. Phase and melting relations, radial reference profiles, and composition

The molar fractions of end-members in a solid solution were prescribed explicitly, most importantly by Mg#, which is assumed uniform for unmelted rock but changes on melting and partitioning between perovskite and ferropericlase (cf. Auzende et al., 2008). The proportions of minerals were explicitly prescribed on the basis of experiments by Bertka and Fei (1997). Phase boundary locations were derived from detailed parameterizations of experimental phase diagrams (Katsura and Ito, 1989; Ito and Takahashi, 1989; Katsura et al., 2004) in $(p, T, \text{Mg\#})$ space for the $(\text{Mg,Fe})_2\text{SiO}_4$ system and from a less firmly constrained parameterization of the diagram by Bertka and Fei (1997) and additional data (O'Hara et al., 1971; Bertka and Holloway, 1994; Woodland and Angel, 2002; Ulmer and Stalder, 2001; Gasparik, 2003; Fei et al., 2004) for other systems, for which the chemical relations are more complex and the phase diagrams are less well known. Fig. 2 shows calculated peridotite mineralogies along an adiabat for two Mg# values. In order to capture the potentially dynamically important effect of the basalt–eclogite transformation of crustal material, we parameterized this transition according to the phase diagram for dry MORB from Litasov and Ohtani (2007). In order to determine the initial adiabat at constant entropy S, we performed a 4th-order Runge–Kutta integration of

$$\left(\frac{\partial T}{\partial p}\right)_S = \frac{\alpha T}{\varrho c_p} \tag{10}$$

from a given potential temperature, using the bulk properties and proceeding in small paired steps of isobaric heating and isothermal compression. Temperature shifts in phase transitions were included by using effective values for α and c_p (Christensen and Yuen, 1985), with transition loop widths and Clapeyron slopes taken from our parameterized phase diagrams. As the thermoelastic properties are required at each time step for every grid point, but their

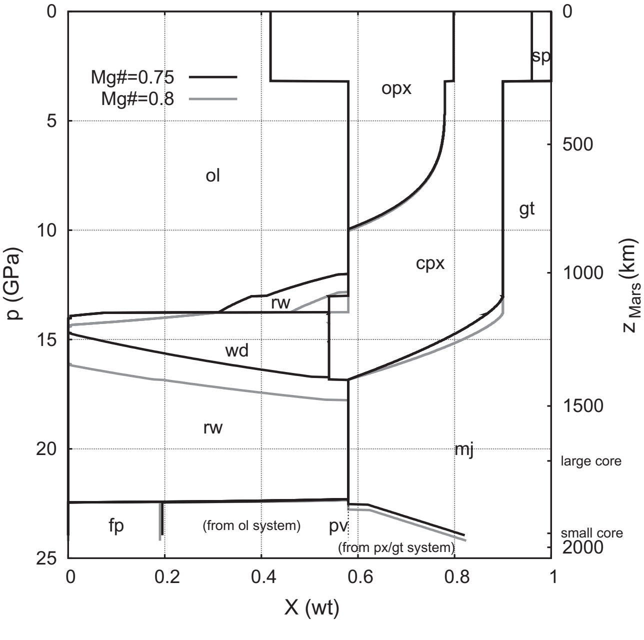

Fig. 2. Mineralogical composition for initial adiabat with a potential temperature of 1773 K for a Mg# of 0.75 (black) or 0.8 (gray) as calculated from the mineralogy parameterization. Mineral names are abbreviated as follows: ol – olivine, opx – orthopyroxene, cpx – clinopyroxene, sp – spinel, gt – garnet, rw – ringwoodite, wd – wadsleyite, mj – majorite, pv – perovskite, fp – ferropericlase.

computation is time-consuming, we interpolated them from a precalculated dataset in $(p, T, \mathrm{Mg\#})$ space.

For use in the convection algorithm, properties must be assigned to a depth in the grid rather than pressure. From the mass and rotational period of the planet and the fact that, for a spherically symmetric mass distribution, g at a given depth depends only on the mass at greater depth, we calculated iteratively and simultaneously the depth profiles of lithostatic pressure and g, starting at the top and proceeding downward in small steps of thin spherical shells of homogeneous density. This procedure ensured that relations among lithostatic pressure, g, and depth were consistent with each other and with the mineralogical model and gives results that are in good agreement with independent calculations, e.g., by Sohl and Spohn (1997).

Depth profiles of some thermoelastic properties and of gravitational acceleration at 4 Gy model time from a few representative models are shown in Fig. 3 for the four combinations of Mg# and potential temperature. The profiles for density and g agree quite well with the sublithospheric parts of those of Sohl and Spohn (1997), whereas $\alpha(z)$ shows a bit more variation and $k(z)$ is somewhat higher in our models, but within a range similar to the independent calculations of Keller and Tackley (2009), both of which used a somewhat simpler parameterization of material properties.

We used experimental results by Bertka and Holloway (1994) and mineral melting proportions from Kostopoulos and James (1992), expressed in terms of melting degree f, to estimate changes in mineral proportions and account for phase exhaustion due to melting, all of which are poorly known, especially above ~2 GPa. For melting-related changes in major-element chemistry, we concentrated on iron content, because this parameter most affects density. The Mg# of the residue is calculated from f and empirical Mg–Fe distribution coefficients (Råheim and Green, 1979; Langmuir et al., 1992; Jones, 1995; Toplis, 2005; Mibe et al., 2006a).

As internal heat sources we considered the long-lived radioisotopes ^{40}K, ^{232}Th, ^{235}U, and ^{238} U, which are strongly incompatible. The partition coefficients for the minerals (Hauri et al., 1994; Harlow, 1997; Blundy and Wood, 2003; Mibe et al., 2006b) from which the bulk coefficient for the local mineral assemblage was determined were generally taken as constant. Partitioning was calculated from f for non-modal, nearly fractional melting (Shaw, 1970). The concentrations of these radionuclides due to partitioning and radioactive decay are represented by tracer particles, after Xie and Tackley (2004). Most of our models use the radionuclide values from Wänke and Dreibus (1994) (hereafter abbreviated WD), but we also tried the concentrations from Lodders and Fegley (1997) (hereafter LF), with a potassium content about three times higher than WD.

Melting degree was parameterized as a function of a p-dependent normalized temperature as in Katz et al. (2003) and Ruedas (2006) for terrestrial lherzolite, i.e., as a continuous sequence of concave-up curves spanning the interval between the bulk solidus and the melting curve of the solid phase in equilibrium with the melt at the liquidus, i.e., forsterite, pyrope, or periclase in order of increasing p; kinks appear at points of phase exhaustion. We adjusted the parameters to the different melting behavior of martian peridotite, constrained by the study of Bertka and Holloway (1994), from which the temperature interval between the solidus and exhaustion of clinopyroxene is narrower for Mars, at least for spinel lherzolite; we assumed that this holds true also for garnet lherzolite. The dry solidus was parameterized using data from Bertka and Holloway (1994) and Schmerr et al. (2001):

$$T_s = \begin{cases} 0.10844p^3 - 6.29339p^2 + 132.565p + 1361.63 & \text{for } p < 23\ \text{GPa} \\ 62.5p + 960.5 & \text{otherwise,} \end{cases} \tag{11}$$

with p in GPa and T_s in K. For the liquidus, experimental data for forsterite, pyrope, and periclase were parameterized in a similar form. The solidus and liquidus parameterizations also allow an estimate of latent heat of melting L from their slopes. At the (fertile) solidus and at the liquidus, L can be expressed by a relation analogous to the Clausius–Clapeyron equation for pure substances:

$$L = T_s \Delta V \frac{\mathrm{d}p}{\mathrm{d}T_s}\bigg|_f . \tag{12}$$

ΔV is understood to be the difference between the molar volumes of the bulk solid and liquid, in the spirit of Walker et al. (1988), although a detailed implementation of their method is beyond the scope of this model. The slope of the solidus for residual mantle at a given f was estimated as the average of those of the fertile solidus and the liquidus at p, weighted by f. The volume contrast between solid and liquid was determined from the precalculated solid density and a third-order Birch–Murnaghan equation of state with material parameters for basaltic melt estimated from Ohtani (1984), Courtial et al. (1997) and Jing and Karato (2009).

Melting degree must be tracked during the evolution of the model, because it controls the dynamical behavior of the system through the buoyancy and the distribution of internal heat sources. We adapted the tracer ratio method described by Tackley and King (2003) for this purpose. Melt in excess of a certain threshold melt content was always extracted instantaneously and added to the top of the crust, if its density is smaller than that of the matrix and no stretches of subsolidus material separate it from the base of the lithosphere, whereas other melt was retained in situ. Experimental work and field observations indicate that the threshold lies at 1–2% melt (e.g., Forsyth et al., 1998; Faul, 2001; Seyler et al., 2001), so we chose a value of 1.5% in most models. Negative values of f are interpreted as basalt enrichment, on the grounds that the martian crust is generally basaltic (e.g., Taylor and McLennan, 2009). The basaltic component of the convecting medium was not treated thermochemically in as much detail as the peridotite but was considered as an anomalous material with a different density and viscosity, and changes in density and viscosity due to the basalt–eclogite and eclogite–perovskite transformations (Mackwell et al., 1998; Jin et al., 2001; Kubo et al., 2002) were taken into account by adding a constant to the density and multiplying the viscosity by a constant factor according to the prevailing p and T conditions.

The generation or crystallization of melt is implemented in a similar manner as, for instance, in the work by Hernlund and Tackley (2007) or Keller and Tackley (2009), although with the more detailed descriptions of melting degree and latent heat outlined above. At any pressure and (supersolidus) temperature, the mantle material should have a certain melting degree according to the aforementioned parameterization. If the advected melting degree is larger than the one given by the parameterization, as much of the available retained melt as necessary to remove the difference crystallizes; in the opposite case, more mantle material melts until the expected value is reached. If the amount of melt thus formed exceeds the retention threshold and has negative buoyancy, the excess melt is extracted as described in the previous paragraph, carrying heat with it away from the mantle source. The generation or crystallization of melt thus also causes a decrease or increase of temperature, respectively, which is accounted for via Eq. 12 and a local heat capacity determined from the thermodynamic algorithm. It should be emphasized that the addition of the extracted melt to the surface, i.e., the assumption of 100% extrusive magmatism, is a simplification, so the cautions discussed by Keller and Tackley (2009) apply. In reality, a part of the melt will crystallize within the crust and heat it rather than radiate its heat at the surface, and there will also be some viscous dissipation and conduc-

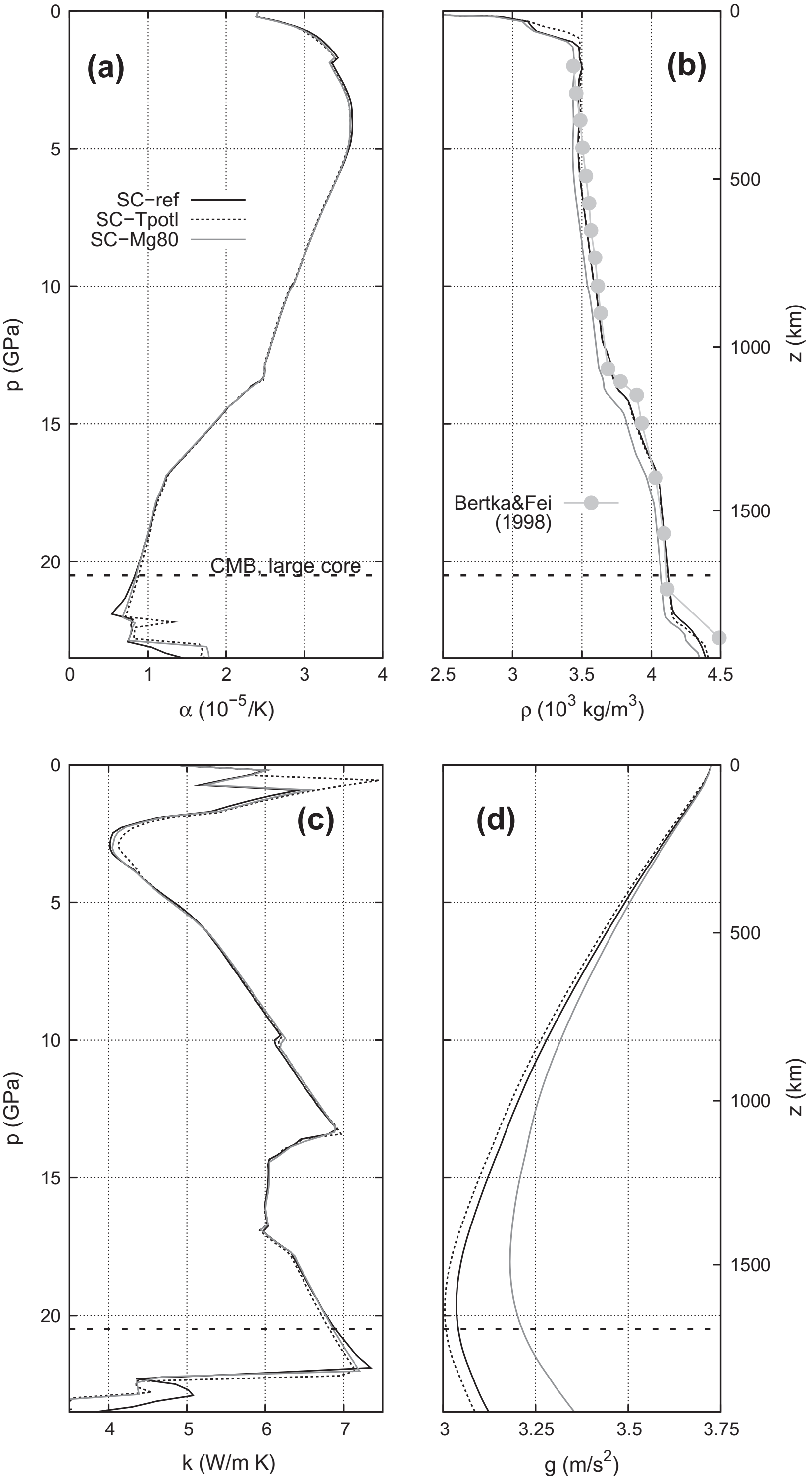

Fig. 3. Final depth profiles of (a) volumetric thermal expansion coefficient, (b) density, (c) thermal conductivity, and (d) gravitational acceleration for the reference small-core model (SC-ref) and for models SC-Mg80 and SC-Tpotl. The dashed line marks the position of the CMB in large-core models. The data from Bertka and Fei (1998) in (b) are based on rock-physical experiments on a WD-like model composition.

tive heating from the flowing melt on its way (e.g., Solomatov and Stevenson, 1993). These contributions to heating are neglected in the present model for lack of reasonably tight constraints on the fraction of intrusive volcanism and because of the difficulty of incorporating a complex, self-consistent description of dike propagation, like the one by O'Neill et al. (2007), in this model. The high eruption efficiency of more than 80% found by those authors lets us expect that the simplification made in our models will not result in a gross underestimate of intracrustal temperatures.

The numerical convection calculations were carried out by solving the equations of conservation of mass, momentum, and energy in the compressible, anelastic approximation (Tackley, 1996; Tackley, 2008). The numerical technique applied resembles that of Xie and Tackley (2004) in most respects, but we used an effective α and

c_p after Christensen and Yuen (1985) for the bulk material as derived from the thermodynamic and petrological model for dealing with the latent heat of phase transitions. As a consequence of the combination with thermoelastic properties, however, the phase transitions vary in space according to local pressure, temperature, and composition. The numerical grid represents a full cross-section through the martian mantle and consists of 512×128 points arranged in a spherical annulus geometry (Hernlund and Tackley, 2008). By using a full annulus we avoided the appearance of cold downwellings that often form preferentially at artificial lateral boundaries.

2.3. Rheological properties and flow law

The viscosity η in our models depends on temperature, pressure, melt and iron content, and mineralogy. We used the general law for diffusion creep given by Hirth and Kohlstedt (2003, Eq. 1), scaled with an additional factor to take into account the effect of an elevated iron content, after Zhao et al. (2009). The resulting flow law is therefore a function of pressure, temperature, porosity (in this case corresponding to the melt content) φ, Mg#, and mineralogy X:

$$\eta(p, T, \varphi, \mathrm{Mg\#}, X) = \eta_{\mathrm{p}}(X)\frac{b^3}{A}\left(\frac{1-\mathrm{Mg\#}_{\mathrm{ref}}}{1-\mathrm{Mg\#}}\right)^{1.5} \cdot \exp\left[\frac{E + pV + c(\mathrm{Mg\#}_{\mathrm{ref}} - \mathrm{Mg\#})}{RT} - a\varphi\right]. \tag{13}$$

For the reference case of a lherzolitic upper-mantle mineralogy, we used the values for olivine as the volumetrically dominant and experimentally best constrained mineral as provided in the cited studies; for this reference case, the petrological term $\eta_{\mathrm{p}}(X)$ is 1. Grain size b was fixed at 1 cm. Deviations from this reference rheology due to the presence of basalt or eclogite or the transition to high-pressure polymorphs were treated by calculating volume-weighted averages with the petrological factors in Table 1. By this flow law the mantle lithosphere is several orders of magnitude more viscous than the asthenosphere and forms a largely stagnant lid.

Table 1
Parameters in Eq. 13

A	$1.5 \cdot 10^9$	Hirth and Kohlstedt (2003), dry diffusion, olivine
E	375 kJ/mol	Hirth and Kohlstedt (2003), dry diffusion, olivine
V	$6 \cdot 10^{-6}$ m^3/mol	Hirth and Kohlstedt (2003), dry diffusion, olivine
a	30	Hirth and Kohlstedt (2003)
b	1 cm	
c	38.35 kJ/mol	
Mg#$_{\mathrm{ref}}$	0.9	Zhao et al. (2009)
$\eta_{\mathrm{p}}(X)$, “petrological factor”		
Lherzolitic upper layer	1	
Basalt	0.25	After Mackwell et al. (1998)
Eclogite	1.2	After Jin et al. (2001)
Lower layer	2.5	After Jin et al. (2001)
Basal layer	10	

3. Results

3.1. Model set-up

The first 500 My of martian evolution were presumably complex and shaped on a global scale by a range of processes, some of which cannot be represented self-consistently within our model setup. The most obvious and arguably most important examples are the multitude of asteroidal and meteoroidal impacts and the possible overturn of the crystallization product of a magma ocean stage (e.g., Elkins-Tanton et al., 2005). These factors yield complicated and poorly constrained initial and boundary conditions. However, at approximately 4 Ga the late heavy bombardment is thought to have largely ended, and martian history seems to have followed a steadier course (e.g., Werner, 2008). Available observations and previous studies provide some guidance for estimating the conditions at that stage. As the modeling approach developed in this paper is already substantially more complex and detailed than that of previous work, we decided to keep the initial conditions simple, start the models at this advanced stage, i.e., at 4 Ga, and explore how well the present state of Mars can be explained with these results. By this approach we do not mean to suggest that the earliest stage of martian mantle evolution has no consequences for how Mars appears today. Rather, our initial conditions can be regarded as representing a hypothetical state in which the early mantle has undergone vigorous convection under the influence of the high mantle temperatures typical for a young planet as well as such processes as a global overturn of the crystallized products of a magma ocean and the thermal effects of several very large impacts, the largest of which are expected to have a major influence on mantle convection patterns (e.g., Roberts and Arkani-Hamed, 2012). One could expect that early heterogeneities are mixed efficiently under such conditions so that the mantle would be homogenized on a large scale after a few hundred million years if the heterogeneities had a sufficiently low viscosity contrast with the ambient mantle and were sufficiently small in spatial scale (e.g., Spence et al., 1988; Manga, 1996). Hence, our approach should implicitly yield an indication of which of the features of Mars have an ancient origin and how much the fingerprint of initial conditions has been obliterated by later processes. The inclusion of the first 500 My is thus largely left to future work.

Given the expected influence of a perovskite-rich basal layer, models were run as pairs, one with a large core (LC, $r_{\mathrm{c}} = 1690$ km, 36.5 wt% S) and one with a small core (SC, $r_{\mathrm{c}} = 1440$ km, 13.5 wt% S). We define a pair of reference models (LC-ref and SC-ref) with some characteristics that are modified in other models. The initial potential temperature T_{pot} is 1873 K, taken from results of van Thienen et al. (2005), Nimmo and Stevenson (2000) and Hauck and Phillips (2002) in expectation that at the model start the mantle should no longer be extensively molten; an alternative model pair (lT) uses $T_{\mathrm{pot}} = 1773$ K instead. Following Williams and Nimmo (2004), a temperature step across the CMB of 150 K was assumed, but we also consider a model pair with no core excess heat (dTc0). There are two reasons to use a superheated core, namely because at 4 Ga the core dynamo is thought to have still been active, and as an aid to support the formation of mantle plumes. In general, we used the core properties as calculated following the procedure from Appendix B. In order to assess the impact of the uncertainty of some these properties on mantle dynamics and observables, we also ran a model pair with the thermal expansion coefficient, heat capacity, and thermal conductivity as given by Williams and Nimmo (2004) (WNc). For the surface porosity, the lower bound of the estimates by Clifford (1993) was assumed, i.e., $\varphi_{\mathrm{surf}} = 0.2$; with regard to the uncertainty in this parameter and the potential impact of the thermal conductivity at the surface (Schumacher and Breuer, 2006), we also ran model pairs with an extreme end-member case $\varphi_{\mathrm{surf}} = 0$ (v0) and the upper bound of Clifford (1993) of $\varphi_{\mathrm{surf}} = 0.5$ (v50). In general, the mantle radionuclide content specified by Wänke and Dreibus (1994) was used, but a model pair with the Lodders and Fegley

(1997) concentrations (LF) was also considered. Mg# was set to 0.75, except for one model pair (Mg80) with Mg# = 0.8 that probes the potential impact of the uncertainty in the iron content of the martian mantle. Melting of the mantle was included in all models except one pair (nomlt), and melt in excess of a fraction of 1.5% was extracted if certain conditions described in Section 2.2 were fulfilled. As this parameter is not precisely known but may influence convection dynamics, e.g., via the density and the viscosity, we also ran models with threshold values of 1% (mx1) and 2% (mx2). In all models, all thermodynamic properties as described in the previous section were considered, and phase boundary effects were taken into account accordingly. In order to probe the influence of phase boundaries with regard to the result of the previous studies, e.g., by Breuer et al. (1997), we also considered a model pair for which the latent heat effects of the solid-state phase boundaries were set to zero (nolat). In an attempt to assess the effect of the crustal dichotomy, we calculated a pair of models including a crustal dichotomy (dcht), which was initialized by removing all erupted melt and thus suppressing crust formation at 40% of the planet's surface until the remaining surface area had reached an average crustal thickness of 60 km; after that, normal crust formation could proceed everywhere at the surface. Finally, one single model, MC-Tpotm/v35, was run in an attempt to produce a basal layer at the brink of disappearance and to improve the match of some results with independent observations; in this model, a core with an intermediate radius of 1565 km and a sulfur content of 25 wt% was used, the mantle T_{pot} was reduced to 1843 K, and the surface porosity was increased to 0.35. An overview of the model parameters is given in Table 2. In addition to those models, we also ran a model pair identical to the reference models but starting at 4.4 Ga with a correspondingly higher concentration of radionuclides in the early martian mantle ("long" models). The purpose of that model pair is to give an impression of how our models would have looked had we not omitted the first few hundred millions of years but replaced them with an evolution that follows from the well-defined initial and boundary conditions used here. Due to the higher initial radionuclide content, internal heating is initially stronger in these models, but in general they do not differ fundamentally from the reference pair, especially as far as present-day observables are concerned. Therefore, we have excluded them from the analysis and refer to them only in the few instances for which a comparison is of interest.

Table 2
Model parameters. Default values of variable parameters are printed in italics, values marked with an asterisk apply only to model MC-Tpotm/v35.

Planetary radius, R	3389.92 km
Total planetary mass, M	$6.4185 \cdot 10^{23}$ kg
Surface temperature	215 K
Mantle	
Mantle thickness, z_{m}	1700 or 1950 km
Initial potential temperature, T_{pot}	1773, 1843*, or *1873* K
Initial core superheating	0 or *150* K
Surface porosity, φ_{surf}	0, *0.2*, 0.35*, or 0.5
Melt extraction threshold	0.01, *0.015*, or 0.02
Bulk silicate Mars Mg#	*0.75* or 0.8
Present-day K content	*305* or 920 ppm
Present-day Th content	56 ppb
Present-day U content	16 ppb
Core	
Thermal expansion coefficient (CMB), α_{c}	$7.4\text{–}8.2 \cdot 10^{-5}$[ab] or $5.85 \cdot 10^{-5}$ 1/K
Average isobaric specific heat, c_{pc}	*750* or 780 J/(kg K)
Thermal conductivity, k_{c}	$\sim$*7.3–19.5*[a,c] or 40 W/(m K)

See depth profiles in Fig. 8 for variables not listed here.

[a] Varies between models and with time; see Appendix B.

[b] Average values lie between 6.39 and $6.85 \cdot 10^{-5}$/K.

[c] Extreme values; lower values apply to LC, larger values to SC models.

The initial conditions appropriate to a numerical model of a planetary mantle are never well-constrained, regardless of whether the model begins "directly after solidification" (probably best defined as the rheological transition from liquid-dominated to crystal matrix-dominated viscosity that occurs at the maximum density crystal packing) or, like in our models, a few hundred million years later. This uncertainty is because the solidification of an early magma ocean is a gradual process that may have involved, among other things, the incorporation into the earliest crust of buoyant cumulate bodies (e.g., Bridges and Warren, 2006) now possibly overlaid by younger material. This earliest crust certainly has been strongly modified at all length scales by multiple asteroidal and meteoroidal impacts spanning a range of magnitudes, of which the larger ones may have remixed crustal material into the mantle and influenced mantle dynamics and melt production on a regional scale (e.g., Golabek et al., 2011). As will be discussed in Section 4.4, estimates even for present-day crustal thickness span a wide range, and specific values for the thickness of the crust in the Noachian are even scarcer, although there is a consensus that a substantial fraction of the crust present today was already in place by the end of the Noachian. The thickness of the magnetized crust, of which the youngest parts would have formed at most a few hundred million years after the start of our models, is estimated to lie between 35 and 55 km in most studies (e.g., Nimmo and Gilmore, 2001; Ruiz et al., 2006a; Voorhies, 2008; Ravat, 2011). A mass-balance estimate derived from ^{143}Nd concentrations gives a thickness of 20–30 km for the earliest crust (Norman, 1999; Norman, 2002). Starting at 4 Ga, successful models should therefore have an initial crust somewhat thicker than the latter value and lying within the range of the estimates for the magnetized crust, under the assumption that most or all of the crust was magnetized at that time.

As the isobaric melting curve is steep at lower melting degrees (Bertka and Holloway, 1994), the uppermost initial temperatures lie relatively close to the fertile solidus. To represent the initial compositional state of the mantle at 4 Ga, i.e., after ~500 My of planetary evolution, and to fulfill the requirement outlined above that a crust of a certain thickness already existed at that time, the model run was initialized with a special calculation that produced this crust and depleted the underlying mantle accordingly as follows. An average $f(z)$ profile for the chosen potential temperature was calculated on initialization and defined the initial condition for mantle composition. The initial temperature profile was an adiabat that was modified according to latent heat consumption when producing melt in the supersolidus regions and merged into exponential temperature profiles at the top and bottom boundary layers. The temperature boundary conditions were given by the average surface temperature of Mars and the temperature at the surface of the core, which subsequently evolved according to the parameterized core model in interaction with the thermal evolution of the mantle. Melt was extracted if a certain threshold porosity of the host rock was exceeded as described in Section 2.2, and all extractable melt was added to the top as an initial crust, i.e., we did not use an initial condition with an overturned mantle and an eclogitic cumulate at its bottom as suggested by Elkins-Tanton et al. (2003). The calculation of melt formation and extraction in this initial stage included the redistribution of radionuclides from a homogeneous concentration into an enriched initial crust and a depleted uppermost mantle. We emphasize that as a consequence of this approach, the initial thickness of the crust is not an input parameter of our models that is explicitly set but follows from other input parameters, in particular from the initial potential temperature. It can therefore be used as a criterion to assess the quality of a model.

3.2. Dynamical and thermal evolution

All models result in the formation of a stagnant lid, which is stabilized by its high viscosity as well as by the lower density of the basaltic crust. This lid experiences long-term growth by thermal conduction, but it is also eroded from below by small-scale convection, as its lower edge becomes gravitationally unstable. The basaltic crust usually grows to a maximum thickness of less than 130 km, which corresponds to a pressure not exceeding ~1.5 GPa. Therefore, it always remains completely within the stability field of dry basalt and does not transform into eclogite, so that crust once formed is gravitationally stable and does not further recycle into the mantle. The two reference models are shown as examples in Figs. 4 and 5 (also see animations in the Electronic supplement).

Melting is an important factor in controlling convection, because it modifies thermal and compositional buoyancy, and the formation and growth of the crust affect the density and velocity structure in the uppermost mantle. Melting-related effects such as the depletion in internal heat sources and the consumption of latent heat contribute to cooling of the uppermost mantle and the growth of the thermal lithosphere more than any of the other parameters considered here. In models without melting, the distribution of radionuclides remains spatially homogeneous, because the incompatible radioactive elements are not extracted with the melt. Because of this immobility of the internal heat sources and the lack of heat removal by erupted melt, no efficient mechanism of heat loss operates, and the deeper mantle heats up over a long time span. Its convective vigor shows little change over the 4 Gy time span.

The mid-mantle phase transitions impose a thermal and rheological layering on the mantle that also influences flow patterns, although the general pattern is whole-mantle convection. The effect of the endothermic phase change in SC models is strong enough to slow down the general flow compared with models in which the thermal effect of the phase transitions was suppressed. The potentially accelerating effect of the exothermic phase transition is less visible. In all small-core models, the basal pv + fp layer does not participate substantially in the convection of the mantle, but remains undepleted and unmolten through the entire 4 Gy timespan; the only exception is model SC-nolat, for which the latent heat effect of the phase transition is absent and the basal layer shows the same degree of depletion as the layer above it. In the other SC models, the melting degree shows a small maximum, just above the basal layer, that corresponds to a similar maximum at the CMB of the LC models; this layer is related to melting at or near the base of plumes, but melt is not extracted from these depths. However, in the “hybrid” model MC-Tpotm/v35 with its intermediate core size, a basal layer with an average thickness of approximately 15–30 km survives until ~3.5 Gy but does participate in whole-mantle convection; its melting degree is virtually the same as that of the overlying lower layer.

In all models, numerous small downwellings descend from the base of the lithosphere at the beginning and cool the mantle, but they do not transport any crustal material back into the mantle. At the same time, various small plumes emerge from the CMB and ascend towards the base of the lithosphere; in the nomlt models, the formation of plumes begins with a delay of several hundred million years. Gradually both the downward flow and the hot plumes become less vigorous, and maximum mantle flow velocities reach present values of a few cm/y or less. Several of the plumes merge and become more stationary, although only a few models eventually form a stable pattern with two or three fixed plumes. Fig. 6 shows a few examples that highlight especially the contrast between LC and SC models with regard to the strength and number of plumes. In LC models, the number of plumes typically drops to about two-thirds to less than half the initial value of 8 to 10 during the 4 Gy of the run. In SC models, the number of fully-formed plumes tends to be lower and changes less through the evolution of the model, and the temperature anomaly associated with them, which is initially a bit lower than in the LC models, also declines less so that SC model plumes are generally hotter relative to their surroundings than LC model plumes after 1 Gy. Even the thin basal layer of model MC-Tpotm/v35 seems to suffice to reduce the number of plumes. In the last ~2 Gy of the modeled time span, plume temperature anomalies do not usually exceed 50 K even in SC models. The change in plume numbers is not a monotonic decrease but more irregular or, in some cases, quasi-periodic, which reflects the unsteadiness of the plumes. In agreement with van Thienen et al. (2006), we find that a superheated core is not necessary for plumes to form.

Otherwise similar models with a Mg# of 0.75 or 0.8 show similar general trends in their thermal evolution (Fig. 7), as do models with different extraction thresholds or surface porosities. Even for models with different radionuclide contents, initial potential temperatures or core superheat, thermal profiles are quite similar through most of the mantle, and most of the differences appear near the boundary layers, where models with higher initial temperatures or heat production remain hotter (see Fig. 8a). This effect is particularly noticeable in the thinner lithosphere of models with LF composition, where the initial high ^{40}K concentration in the young basaltic crust provides substantial heating, and in the nomlt pair, where radioactive heating is homogeneous.

3.3. Melting and crust formation

Rates of melt production and magmatic addition to the crust are highest in the beginning and remain at a fairly high level for 0.5–1 Gy, although the average temperature of the mantle falls below the solidus after a few hundred million years. Early peak depletion values in the sublithospheric melting zone lie between 0.15 and 0.2 in most models and slightly below in the Tpotl models. With time, melting and crust production decrease smoothly, and crust formation essentially ceases at some point between 2 and 3 Gy, although in some of the SC models, some minor increase in crustal thickness can be observed at even later times. In most cases, the basaltic crust grows to a thickness between approximately 30 and 130 km, with final mean values between 75 and 90 km; only in the LF models does the final average thickness exceed 130 km. This final thickness is nearly reached after ~2–2.5 Gy of growth that is uninterrupted but becomes more localized; in all models except the LF pair, thickness growth rates have fallen below 10 m/My for more than 90% of the crust by ~2 Ga. The SC models, in which mantle temperatures fall more slowly, generally approach this final thickness more gradually than their respective LC counterparts, and reach a higher value, although in most cases it is greater by only a few kilometers. Although plumes exist in all models up to 4 Gy, they have become so weak and cool by 2.5–3.5 Gy in most of the LC models that they no longer cross the solidus, so that volcanic activity drops to zero even at the last remaining volcanic centers at that time. As a consequence of this evolution pattern, most of the crust is therefore Noachian in age ($\gtrsim$3.7 Ga), some Hesperian (~3.7 to ~2.9 Ga), but only a small fraction is Amazonian ($\lesssim$2.9 Ga) (epoch boundaries from Taylor and McLennan, 2009). The thinned-crust area in the dcht model pair starts with a thickness difference of 60 km compared with the normal crust, but it “catches up” so that the final crustal thickness contrast between the two domains is only ~15 km. Convective mixing reduces the average melting degree of the mantle to fairly constant levels of a few percent at depths greater than the base

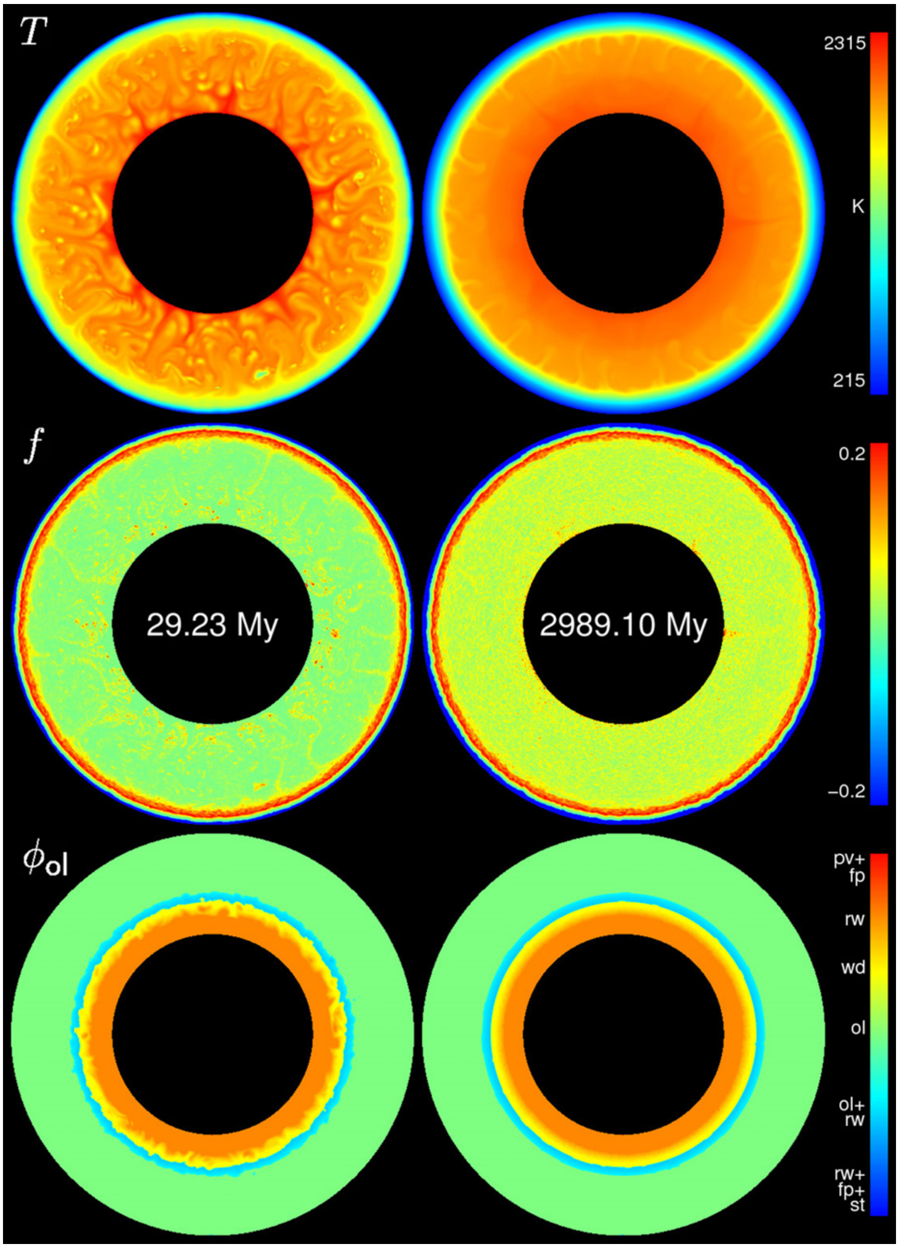

Fig. 4. Snapshots of temperature, melting degree, and $(Mg,Fe)_2SiO_4$ phases in the large-core reference model (Model LC-ref) at 29 and 2989 My. Animations of the evolution of these variables as well as viscosity, ^{40}K concentration, and other phases for the entire model run are provided in the Supplementary material. See online version for color image.

of the melting zone, whereby models with higher temperature or heating have slightly higher melting degrees (Fig. 8b).

Initial potential temperature and radionuclide contents are the most important parameters controlling the thickness of the crust. The more strongly heated LF models produce much thicker crust than the corresponding reference models, especially because the enhanced heating due to the higher ^{40}K content occurs mostly early in the model's evolution. The temperature of the core markedly affects the final crustal thickness only in the SC case; model SC-dTc0 has a final mean thickness 12 km greater than the reference case. Other factors such as Mg#, the threshold for melt retention, or the void fraction of the uppermost crust, which influences thermal conductivity, have only minor or even negligible influence on crustal thickness, with variations of a few kilometers between the final values of the corresponding models.

3.4. Mantle properties

As the thermal state of the mantle controls mineralogy, changes in temperature alter the relative volumes of the different layers. In particular, cooling of the mantle overall leads to an expansion of the lower layer at the expense of the upper and, if present, the basal layer in most cases. Initial cold downwellings from the lithosphere often cause transient cooling in the upper part of the mantle that lets the lower layer shrink temporarily before expanding again, whereas the basal layer undergoes its most substantial reduction in the first 1 Gy and does not change much thereafter. However, these variations have a magnitude of 1% or less.

The laterally averaged viscosity profiles are mostly controlled by temperature, except for the crust, where the presence of basalt is assumed to result in a lower viscosity in spite of low tempera-

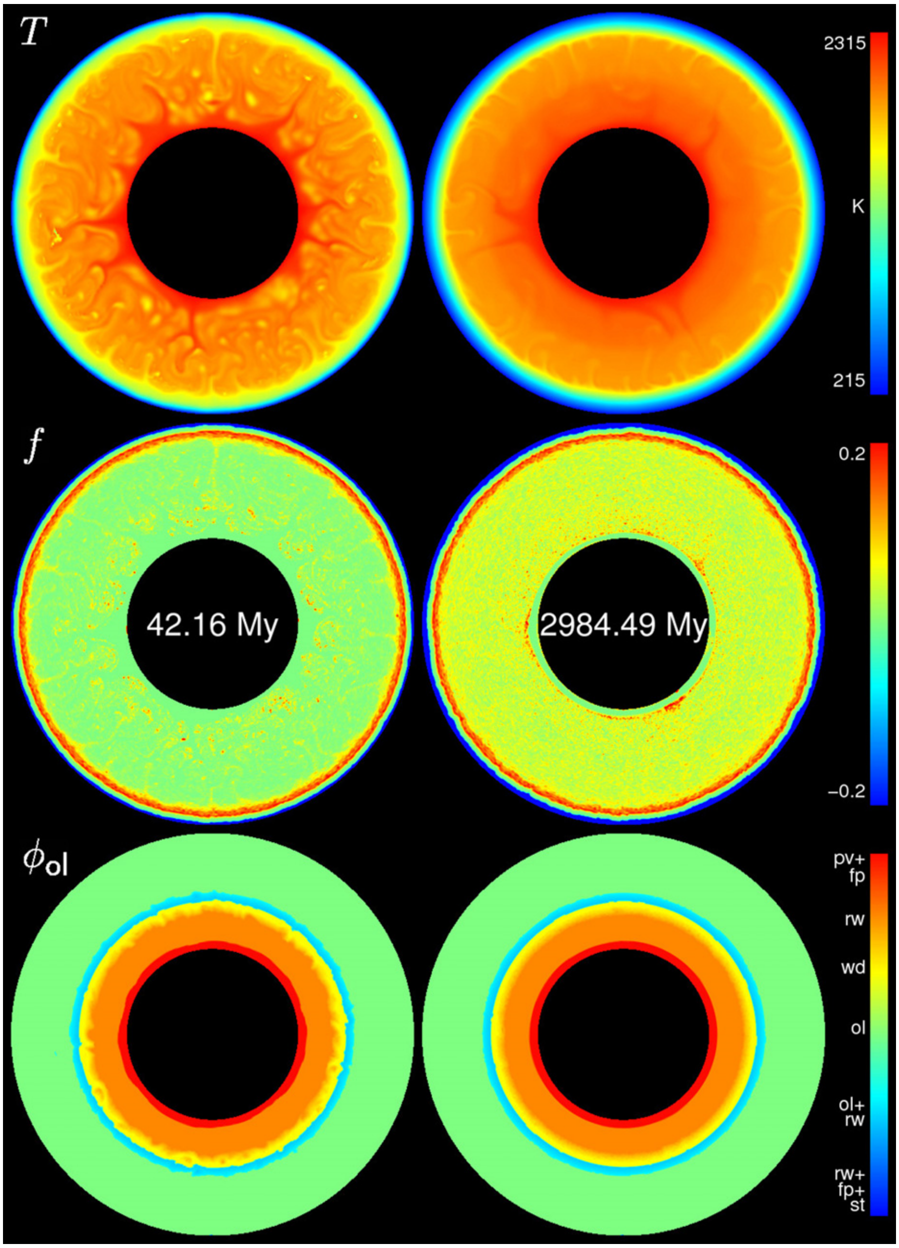

Fig. 5. As in Fig. 4, for the small-core reference model (Model SC-ref) at 42 and 2984 My. Corresponding animations are available in the Supplementary material. See online version for color image.

tures. In general, models with higher temperature in the convecting mantle result in a thinner lithosphere. η varies with depth by about two orders of magnitude in the sublithospheric mantle and shows a small increase at the mid-mantle phase transitions (Fig. 8c). The small-core models have an additional viscosity peak due to the mineralogy of the basal layer.

3.5. Radionuclides

The concentrations of ^{40}K, ^{232}Th, ^{235}U, and ^{238}U fall to about 10%, 80%, 2%, and 55% of their initial values, respectively, over 4 Gy, and radioactive heating is greatly reduced after the first 0.5–1.5 Gy, especially in the LF models. The average depth profiles of their concentrations anticorrelate with the average $f(z)$ (Fig. 8b and d). Crustal concentrations rapidly reach values one to two orders of magnitude higher than in the upper sublithospheric mantle from which radionuclides are extracted and where convective mixing soon leads to fairly homogeneous concentrations somewhat below the WD or LF reference values. The average surface concentrations do not vary greatly between the different models, but they do show a moderate systematic variation with the extraction threshold, and in the LC subset the surface concentrations are notably higher in the models with low temperature, LC-Tpotl and LC-dTc0, presumably because there is a smaller amount of melt to carry and dilute the extracted incompatible elements. In general, average crustal concentrations are slightly higher in LC models than in SC models. In all models most of the radionuclide inventory of the bulk silicate planet remains in the mantle. The final crustal fraction of radiogenic elements lies between 10% and 15% for most models and slightly exceeds 20% in the LF models, and it tends to be a few percent lower in small-core models in comparison with their large-core counterparts. This fraction evolves in correlation with crustal

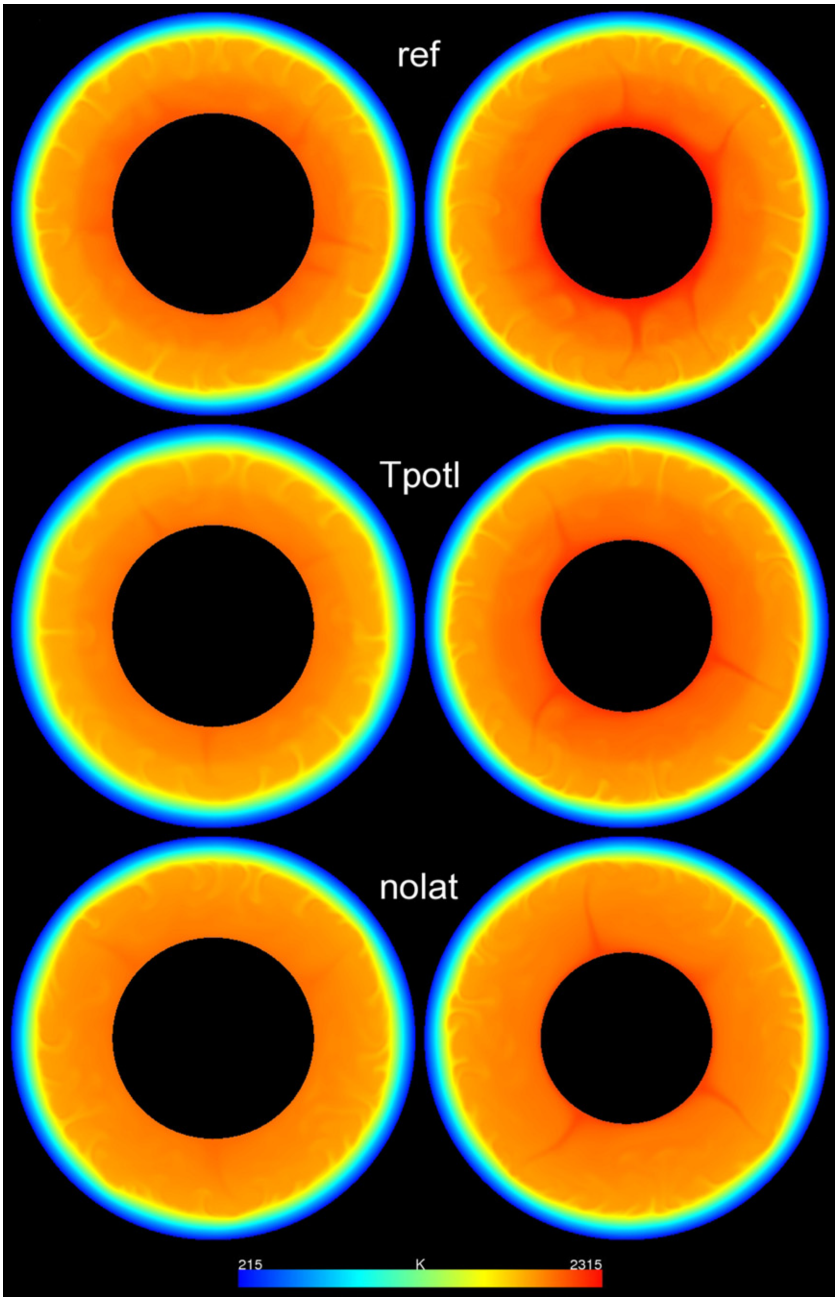

Fig. 6. Snapshots of temperature at 4 Gy of the reference, Tpotl, and nolat model pairs. See online version for color image.

thickness and lies substantially below the value suggested by Kiefer (2003).

4. Discussion

4.1. Dynamical and thermal evolution

Comparison of the reference models with the nolat models, in which the Clapeyron slope of the phase transitions was set to zero, indicates that phase changes do not present a major obstacle to whole-mantle convection in Mars, although some influence on the temperature distribution and on the vigor of convection can be observed, the latter especially in the case of the endothermic transition near the CMB. Neither do other effects of the phase transitions, e.g., the changes in density and viscosity, result in layered convection. Some earlier studies (e.g., Breuer et al., 1997) found partial layering even in models that included only an exothermic phase boundary. These authors offered as an explanation for this somewhat counterintuitive observation that latent heat consumption on plume ascent overcomes the buoyancy effect under the smaller g and pressure gradient than for Earth. We find the net effect of the mid-mantle transitions to be generally rather weak, and we do not see evidence for any appreciable layering effect of those transitions. The reason probably lies in the effect of the transitions of minerals other than olivine, which have Clapeyron slopes opposite to those of olivine at similar depths (e.g., Yusa et al., 1993; Gasparik, 2003) and hence may offset their effect to some extent; these transitions were not included in the earlier studies. Furthermore, the width of these transitions is narrower in the study of Breuer et al. (1997) than in ours, so that the latent heat effects

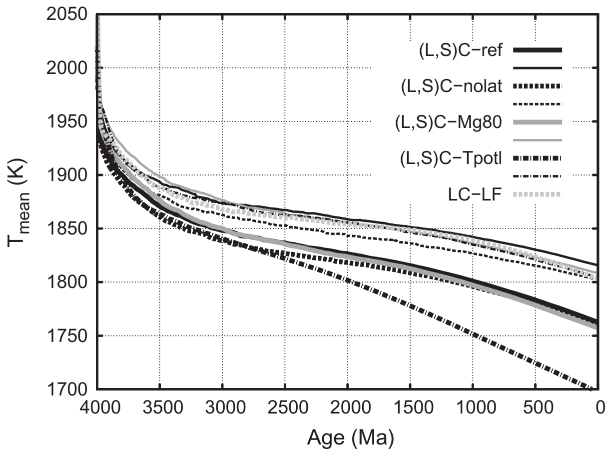

Fig. 7. Mean mantle temperature as a function of time for selected models. Thick lines designate models with a large core, thin lines models with a small core.

are spread out over a larger volume in our models and may therefore be weaker.

Although plumes form in all of our models, we find that the existence of a basal pv + fp layer is conducive to stabilizing them and enabling a small number of long-lived plumes hypothesized as an explanation for Tharsis and Elysium. However, the evolution towards a small number of plumes is a slow and unsteady process that can cover a major part of the entire lifetime of the model even in those few models in which a stable final configuration is reached; although this is shorter than the multi-billion-year timescale of Harder (1998), it is still too long to explain the existence of the major volcanic centers of Tharsis and Elysium (e.g., Phillips et al., 2001). On the other hand, Michel and Forni (2011) find degree-one convection neither in large-core models without a basal layer, nor in small-core models with a basal layer, with only one exception; in this exception, the plumes appear at the poles, which indicates that their formation may have been facilitated by the artificial boundary of the axisymmetric spherical grid they use (e.g., van Keken, 2001). One possibility to resolve the problem with the superplumes is that dense eclogitic remnants from an early mantle overturn, which was not included in our models, accumulate at the CMB, stamp out plumes in some areas, and possibly sweep hot material from the thermal boundary layer together in a way that promotes the formation of a smaller number of plumes in a limited area. It must also be kept in mind that, in spite of our attempts to base our rheological law on experimental data, the viscosity – especially of high-pressure phases – remains poorly constrained but nonetheless exerts a strong influence on the wavelength of flow patterns. A downward increase of viscosity has promoted the formation of long-wavelength flow patterns in models for Earth's mantle (e.g., Hansen et al., 1993) and facilitated degree-1 convection in models for the martian mantle that have been invoked to explain the origin of the crustal dichotomy (e.g., Roberts and Zhong, 2006; Keller and Tackley, 2009). Alternatively, other possibilities such as subtle effects of variable thermal conductivity in the uppermost mantle (e.g., Schott et al., 2001; Schumacher and Breuer, 2006) or the influence of the dichotomy (van Thienen et al., 2006) could be considered, although we did not observe that the presence of a dichotomy reduces the number of plumes in our tentative dcht model pair. In this context it must be emphasized that all plumes are not created equal: in all models, there are plumes of varying sizes, some stable and almost fixed, others more transient and mobile and more likely to merge. The number of plumes as such should therefore not be assumed equal to the number of isolated volcanic centers; in particular, the mere existence of two large volcanic centers, Tharsis and Elysium, does not by itself mean that there are only two plumes. It would be sufficient if the upper mantle beneath such a province is kept above the solidus sufficiently long to build the volcanic structures observed at the surface by some sort of plume activity, be it in the form of a stable, long-lived superplume or in the form of a group or succession of smaller plumes of shorter lifetime. It should be kept in mind that there is no direct observational evidence for superplumes in the martian mantle that would enforce the existence of two such structures as a firm constraint on any model, and it is worth noting that recent analyses of volcanic structures (Neukum et al., 2010; Robbins et al., 2011) point to a more episodic and spatially variable character of activity in the volcanic provinces. The style of plume dynamics in our models is more compatible with such an unsteady pattern of activity, and while they display progressive localization of volcanism, their unsteady character also allows for the appearance of additional, shorter-lived volcanic centers, for which there is evidence on Mars. Our models also indicate that the time of the transitions from global volcanism to localization at volcanic centers to complete extinction is sensitive to mantle temperature and can vary by billions of years.

The core of Mars is thought to have been superheated as a consequence of planetary differentiation, and this superheat was possibly a major, although not necessarily the only, driving force for the early dynamo. It is difficult to estimate how much of the excess heat was still left at 4 Ga, but especially if the bottom of the mantle had not been extensively molten, it is probable that the superheat had not been consumed entirely at that time (Monteux et al., 2011), because the dynamo may still have existed (if not for much longer). Estimates of its magnitude are difficult even for the stage immediately following planetary differentiation. For this stage, a mean temperature increase of the planet of 300 K (Solomon, 1979) is often cited and suggests that the superheat of the core was markedly higher than this value. In the case of an early mantle overturn, the contrast between mantle and core may have exceeded 1000 K (Elkins-Tanton et al., 2005), although our model setup does not include this process and should therefore not involve such an extreme superheat. Other studies considered a temperature excess of at least 150 K (e.g., Williams and Nimmo, 2004) or even 250 K (e.g., Breuer and Spohn, 2003). Our choice of 150 K for most models is therefore an attempt to strike a compromise and to allow for the existence of a thermal dynamo at least at the beginning of the models as well as foster the formation of plumes that would have been formed before 4 Ga above the still hotter core in the real planet. One of the purposes of the model pair dTc0 is to assess the importance of core superheat for our model predictions and be able to correct possible over- or underestimates if our choice turns out to be too high.

Our models show that a superheated core is not necessary for the formation of plumes, suggesting that the plumes may be at least partly a return-flow phenomenon related to cold downwellings of lithospheric mantle rather than the result of a basal thermal boundary layer (cf. van Thienen et al., 2006); however, the cold downwellings in our models are structures of a rather small size and do not have the character of cold counterparts to the hot ascending plumes. Contrary to the conclusion of Schott et al. (2001), we do not find that strong depletion of the upper layer completely suppresses plume ascent; the reason may be that those authors started with higher initial temperatures that result in stronger depletion and neglected removal of internal heat sources from that layer. Whereas we also observe a strong decrease in flow velocities at the depth of the depleted layer, this decrease seems to be caused by the proximity of the stiff thermal lithosphere, which eventually engulfs the former melting zone, rather than by melting-related compositional layering in the upper mantle.

Breuer and Spohn (2006) observed an increase in mantle temperature over the first ~1.5 Gy and found that for models without

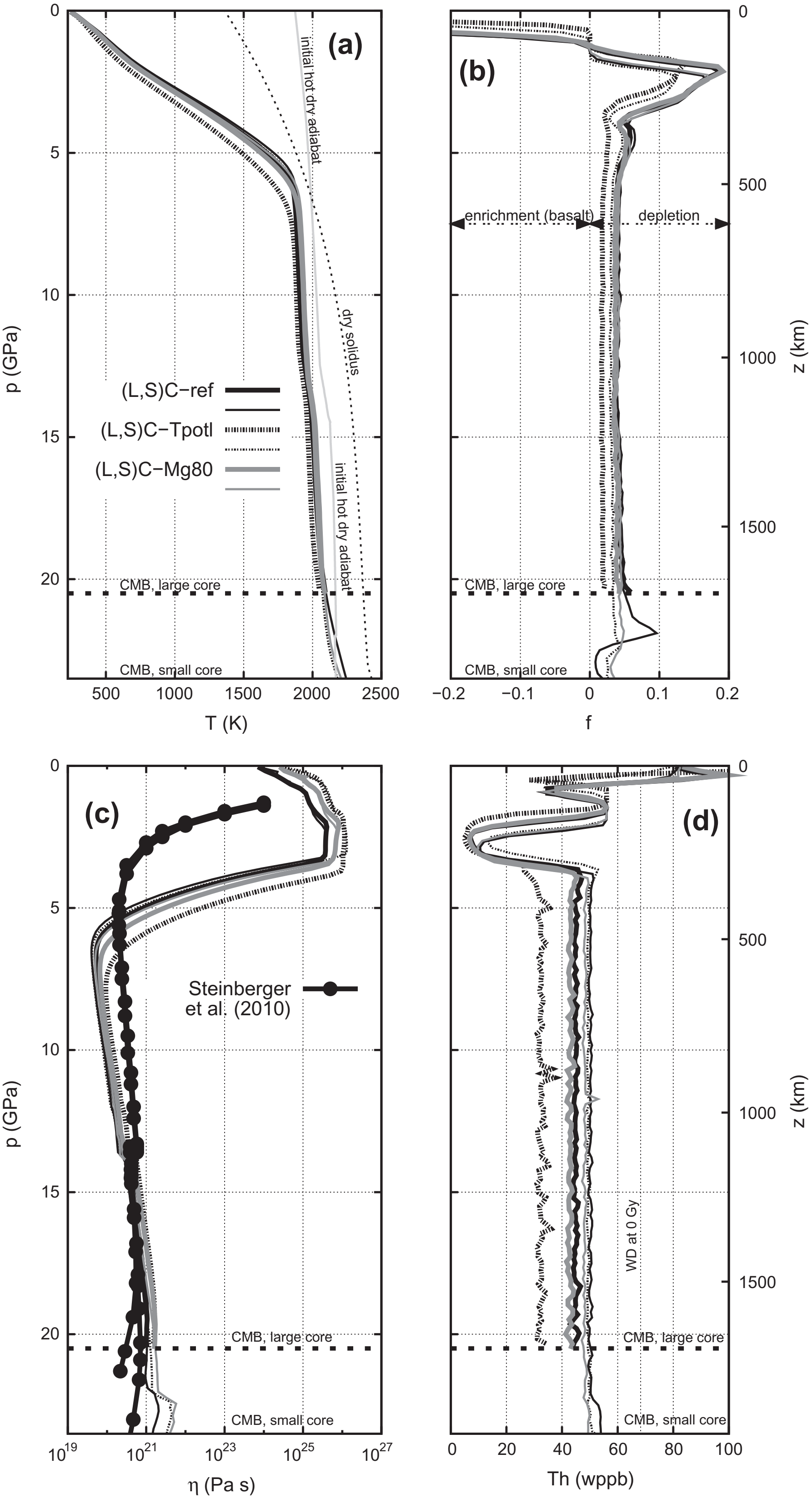

Fig. 8. Horizontally averaged profiles of model parameters versus pressure/depth for three model pairs (large core: thick lines; small core: thin lines) with different Mg# (0.75: black; 0.8: gray) and initial potential temperatures at 4 Gy: (a) temperature, solidus, and hot initial adiabat; (b) melting degree (depletion) f, with enrichment ($f < 0$) indicating increased basalt content; (c) viscosity; (d) ^{232}Th concentration. The viscosity plot also includes $\eta(z)$ models after Steinberger et al. (2010); note that absolute viscosities were not constrained in their study.

a superheated core, the heat flow at the CMB could be close to zero or be directed into the core. Our models start at a later point with artificially simple initial conditions, so a direct comparison cannot be made; the only models in which we see a comparable intermediate temperature increase and an extended period of heat flow into the core are those with suppressed melt production (nomlt), which lack the extraction of heat with the melt. Nonetheless, we can confirm that the heat flow in models without a superheated core (dTc0) is at most approximately equal to that of other models and drops to values close to zero early on. Moreover, heat flow across the CMB is generally very low in small-core models, and there is never enough total entropy available for magnetic field generation, whereas most of the large-core models could sustain a dynamo for a few hundred million years after the start of the model at 4 Ga. Such a result is consistent with estimates for the duration of the martian dynamo but not with the time at which it is thought to have operated. The shorter lifetime of the dynamo in model LC-dTc0 hence indicates that the core superheat at 4 Ga was probably somewhat lower than 150 K. The "long" models, which started with a superheat of 150 K at 4.4 Ga, support this conclusion: while the core hardly cools in the SC case, the timescale for cooling in the LC case is similar to that in LC-ref, indicating that the core would need several hundred millions of years to lose all of its excess heat. In the "long" LC model, the dynamo would go extinct at the time of the Noachian–Hesperian transition, in LC-ref a bit later. The low CMB heat flows, which are of the order of a few mW/m^2, and the rather short duration of the dynamo agree well with the core thermal models by Williams and Nimmo (2004). In the small-core models, the reason for the very low heat flow is likely the dynamic stability of the dense basal pv + fp layer, which preserves its radionuclide content and has a relatively low thermal conductivity; all these factors combine to insulate the core from the mantle and prevent it from cooling as efficiently as in the LC models, in which the temperature at the CMB decreases by more than 200 K in some cases. The resulting present CMB temperatures of $\sim$2050–2120 K for the LC models (except LC-LF) and MC-Tpotm/v35 agree well with the upper bound of $\sim$2120 K from dynamo constraints by O'Neill et al. (2007), whereas the SC models exceed this bound by tens of degrees (cf. Fig. 8a). The insulating effect of a dynamically stable basal layer was also observed by Michel and Forni (2011).

Various authors have concluded that a basal layer may have existed for some time during the history of Mars. Our SC models indicate that the variation in thickness of the layers, including the basal layer, is very small. The disappearance of a basal layer since the Noachian hence requires a quite special combination of mantle temperature and core radius, such as the one implemented in model MC-Tpotm/v35, which was designed for this effect to occur. The model series from Michel and Forni (2011) also suggest that the disappearance of the basal layer requires rather special circumstances. In their study, such disappearance occurs at 3.1 Ga and seems to be linked with the emergence of degree-1 convection, whereas in our model MC-Tpotm/v35 the late disappearance of the layer does not allow us to observe if degree-1 or degree-2 convection will eventually develop. At any rate, it is more likely that a basal layer has either always or never existed in the past 4 Gy. Its disappearance does not seem to have any immediate or obvious effect on core energetics.

The mantle cools by $\sim$100 K within a few hundred million years and at a lower rate thereafter (Fig. 7). Our models indicate that it is possible that temperatures around 1600 K prevailed at a pressure of $\sim$1.2 GPa in the melting zone of the martian mantle at about 4 Ga, as suggested by Lee et al. (2009) from thermobarometry, but not much later in martian history. In an independent thermobarometric study, Filiberto et al. (2010) and Filiberto and Dasgupta (2011) suggested a mantle potential temperature between 1716 and 1803 K for the Noachian mantle and estimated initial melting pressures of the basalts probed by the Mars Exploration Rovers of 2.7 to 5 GPa. The pressure range is compatible with the onset of melting in normal mantle in the early stages of our models, but their temperature estimates lie close to the lower end of the T_{pot} range considered here or even lower. A possible reason may be that the parameterization of the solidus used by those authors lies slightly lower than ours and is calibrated only for $p \lesssim 5$ GPa instead of spanning the full p range of the martian mantle. High temperatures imply a deep onset of melting, in agreement with Draper et al. (2003), who suggested that partial melting on Mars took place in the garnet–majorite stability field. Our models indicate that such deep melting took place at least during the first few hundred million years, especially in plumes. The core also remains hot, especially in the SC models, in which the basal layer insulates it to some extent, and it never begins to crystallize, which is consistent with the absence of a dynamo.

The formation of a stagnant lid that has been stable for at least 4 Gy agrees with the interpretation of the geological record inferred from spacecraft imaging. The consequence that crust has not been recycled implies that any mantle heterogeneity with a crustal signature would have to be ancient and fall within the first few hundred million years of planetary evolution. This inference would support the interpretation of the variability of certain isotope systems in SNC meteorites as a fingerprint of an early crust that has undergone a global overturn (Brandon et al., 2000; Debaille et al., 2009). With regard to the omitted initial 500 My and the assumed simple initial conditions, an implication is that at least some of the complex processes of that early phase have produced large and highly viscous compositional heterogeneities and that the vigor of martian mantle convection had already declined sufficiently at the Noachian–Hesperian boundary for such heterogeneities not to have been mixed into the ambient mantle by the present.

4.2. Surface heat flow and lithospheric thickness

From our modeled temperature–depth profiles, we can approximate the vertical temperature gradient and hence the heat flow q from the temperature of the uppermost grid row. During the vigorous early cooling phase with high heat flux lasting $\sim$500 My, q values drop to average values between approximately 35 and 20 mW/m^2 and decrease more slowly thereafter to 10–25 mW/m^2 (Fig. 9); the value is sensitive to crustal thermal conductivity via crustal porosity, but to none of the other parameters considered here. The heat flux may differ slightly if intracrustal heating due to intrusive emplacement of melt were taken into account, but it is difficult to assess whether the increase in the thermal gradient would enhance the heat flux or whether the effect on the thermal conductivity would reduce it. Heat flow has been inferred from observations of gravity and topography to lie at 30–40 mW/m^2 or more for the ancient southern highlands during the Noachian (McGovern et al., 2002), but corresponding values from lithospheric loads of Amazonian or Amazonian–Hesperian age are $\lesssim$25 mW/m^2. Ruiz et al. (2006a) deduced that Noachian q exceeded 47–68 mW/m^2 for several southern highland regions at the time of loading if half of the heat flow was provided by crustal heat sources. For the north polar region, Ruiz et al. (2010) put an upper limit of 19 mW/m^2 on the present heat flow, and a comprehensive analysis of heat flow estimates for several regions and times by Ruiz et al. (2011) indicated that the global mean value lies between approximately 10 and 22 mW/m^2. The lower values correspond to models with inefficient heat loss and led these authors to the conclusion that Mars may have maintained fairly high internal temperatures.

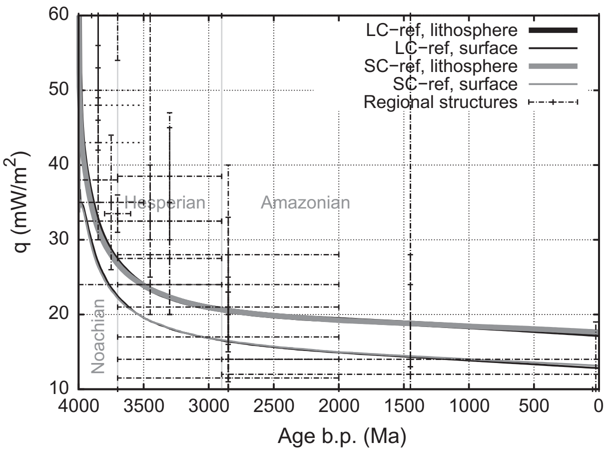

Fig. 9. Mean lithospheric and surface heat flux as a function of time for the reference models. Also plotted are estimates for regional heat flows from other studies (McGovern et al., 2002; Grott et al., 2005; Grott et al., 2007; Ruiz et al., 2006a; Ruiz et al., 2006b; Ruiz et al., 2008; Ruiz et al., 2009; Ruiz et al., 2010; Kronberg et al., 2007; Schumacher and Zegers, 2011); the ages are defined in terms of the estimated duration of the geologic epoch, unless specific ages were given by the respective authors.

All of these heat flow estimates were determined from lithospheric flexure models, a non-Newtonian ductile flow law, and thermal gradients estimated from the difference in temperature between the surface and the base of the mechanical lithosphere defined with that flow law. As those lithospheric thicknesses range from 150 to 300 km, the resulting gradients are lower than ours derived from temperatures in the uppermost crust. To facilitate at least a qualitative comparison, we adopt a similar viscous flow law for dry olivine or diabase and lithospheric stresses on the order of 10 MPa to define the base of the mechanical lithosphere in the manner of Ruiz et al. (2006a). The base of the mechanical lithosphere would then lie near the 900- or 1000-K isotherm, our calculated temperatures (Fig. 12) would yield lithospheric thicknesses that fall within the bounds of these independent estimates but are also consistent with the stagnant lid thicknesses between 300 and 400 km calculated by Schumacher and Breuer (2006). The resulting heat flow values would be similar to or slightly lower than those reported from flexure models, but a few mW/m^2 higher than the value calculated for the surface layer alone, because an average thermal conductivity is used in which the higher conductivities deeper in the lithosphere overcompensate the low values close to the porous surface. These heat flow values also support the suggestion by Ruiz et al. (2011) that Mars has not cooled markedly during its history. All of these heat flow estimates have been inferred from remote observations and necessarily involve assumptions, e.g., about the elastic properties of the lithosphere. A better comparison of our modeled heat flow as derived from the near-surface gradient would be possible with data from an instrument that can measure crustal temperature in situ. The Heat Flow and Physical Properties Package (HP^3) experiment on the InSight mission (Spohn et al., 2012) is expected to fill this gap.

4.3. Radionuclides

Our melting algorithm redistributes radioactive heat sources and hence allows estimates to be made of surface and mean crustal abundances, most of which are listed in Table 3 for K and Th and plotted in Fig. 10. These results can be compared with measurements, of which there are three different types: in-situ measurements by landers and rovers, remote measurements from orbiting spacecraft, and meteorite samples. A selection of these data is given in Table 4 and in Fig. 10 as averages from several individual data points; gaps in the data were filled using elemental ratios derived from available data. A similar comparison can be made with total U concentrations, but for this element there are many fewer original measurements, and the computed concentrations do not yield independent additional information for the purpose of this study.

Surface concentrations of K have been measured in situ by landers and rovers on both soils and rocks on which surfaces were either abraded, brushed, or left untouched, i.e., on objects manifesting a broad range of states of weathering; Th was derived from K/Th = 4600 for thermal emission spectrometry (TES) surface type 2 surfaces from Taylor et al. (2008). This type of data represents essentially a small set of point measurements in the northern plains on the martian surface and covers a depth range of at most a few centimeters. It spans a wide range of values, including some of the highest concentrations observed. The data collected remotely from orbiting spacecraft cover the full surface of Mars and yield concentrations of a number of elements, including K and Th (e.g., Taylor et al., 2006), but also represent a very shallow depth interval. For our discussion we use only the newer datasets from Mars Express and Mars Odyssey (e.g., Taylor et al., 2006; Taylor and McLennan, 2009; Poulet et al., 2009; Hahn and McLennan, 2010), which have global coverage; the latter seem to have provided useful results for both of these elements, whereas the older data of the Phobos 2 mission (e.g., Trombka et al., 1991) cover only a part of the surface and give implausibly high Th concentrations, although the values for K are consistent with the more recent results. The crustal concentrations of K (2000–6000 ppm, corresponding to 234–702 ppb ^{40}K) and Th (200–1000 ppb) from Mars Odyssey do not span a range of values as wide as the rover data but indicate similarly high concentrations of K and Th at the surface. Furthermore, the estimates of Taylor et al. (2006) for interior abundances favor an Mg# close to 0.75 and K and Th concentrations consistent with the figures of Wänke and Dreibus (1994). The third type of data comes from meteorites considered to be of martian crustal origin. For comparison with our results, bulk compositions are the appropriate subset of data. Usually, at least

Table 3
Approximate average ^{40}K and Th surface concentrations in ppb by weight at 4 Gy from models. CMB depths in the different model series are: LC, 1700 km; MC, 1825 km; SC, 1950 km.

Model	model feature	^{40}K	Th
LC-ref	reference case	47	81
LC-mx1	melt extraction above 1%	45	74
LC-mx2	melt extraction above 2%	50	90
LC-Tpotl	$T_{pot} = 1773$ K	66	106
LC-dTc0	no superheated core	80	117
LC-LF	tripled ^{40}K	102	61
LC-Mg80	Mg#=0.8	47	83
LC-nolat	latent heat of phase transitions = 0	48	84
LC-WNc	different core α, c_p, k (cf. Table 2)	48	82
LC-v0	surface porosity 0%	48	82
LC-v50	surface porosity 50%	49	84
LC-dcht	crustal dichotomy	48	82
MC-Tpotm/v35	$T_{pot} = 1843$ K, surface porosity 35%	47	83
SC-ref	reference case	47	82
SC-mx1	Melt extraction above 1%	43	72
SC-mx2	melt extraction above 2%	49	87
SC-Tpotl	$T_{pot} = 1773$ K	45	79
SC-dTc0	no superheated core	45	77
SC-Mg80	Mg#=0.8	46	83
SC-nolat	latent heat of phase transitions = 0	45	78
SC-WNc	different core α, c_p, k (cf. Table 2)	47	80
SC-v0	surface porosity 0%	49	80
SC-v50	surface porosity 50%	50	82
SC-dcht	crustal dichotomy	47	80

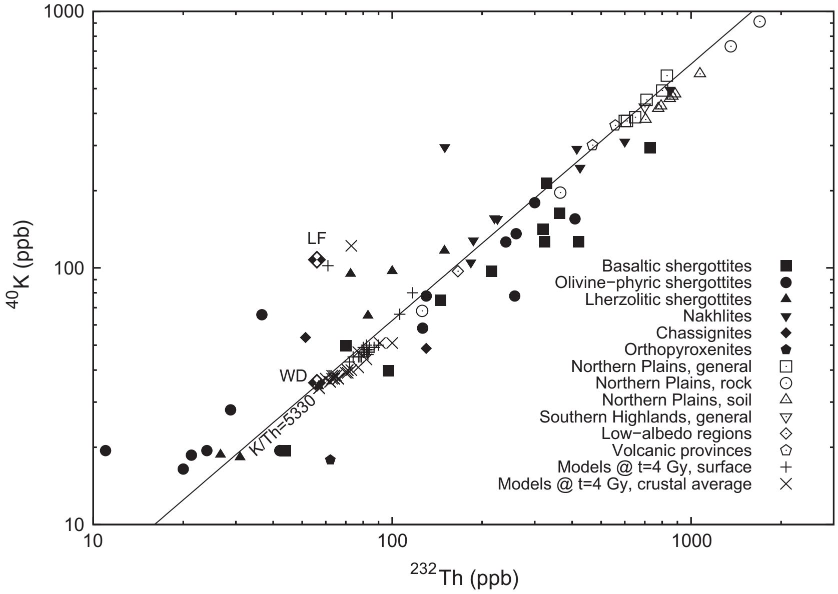

Fig. 10. ^{40}K vs. ^{232}Th for martian meteorites (filled symbols), lander/rover and spacecraft measurements (open symbols), and the models of this study (crosses). Meteorite data (basaltic shergottites: Shergotty, Zagami, EETA79001, QUE94201, Los Angeles, NWA480,856,4468,5298,5990; olivine-phyric shergottites: DaG476,489, Y980459, SaU005, Dho019,378, NWA1068,4480,4925,5789,6162,6234, LAR06319, RBT04262, Tissint; lherzolitic shergottites: ALHA77005, Y793605, LEW88516, NWA1950,6342, GRV99027; nakhlites: Nakhla, Lafayette, Governador Valadares, NWA817,998,5790, Y000593,749, MIL03346; chassignites: Chassigny, NWA2737; orthopyroxenites: ALH84001) are a selection of bulk chemistry data from Meyer (2006) supplemented by data from Wadhwa et al. (2001); Shirai and Ebihara (2004); Ikeda (2004); Imae and Ikeda (2007); Lin et al. (2008); Treiman and Irving (2008); BasuSarbadhikari et al. (2009); Irving et al. (2010a,b, 2011); Weisberg et al. (2010); Kuehner et al. (2011); Hui et al. (2011); Filiberto et al. (2012); Chennaoui Aoudjehane et al. (2012). Lander/rover (Viking 1 and 2, Pathfinder, Spirit, Opportunity) and spacecraft (Mars Express/OMEGA, Mars Odyssey/GRS) data are from Foley et al. (2003), Meyer (2006), McSween et al. (2006), Boynton et al. (2008), Taylor and McLennan (2009), Poulet et al. (2009), Schmidt and McCoy (2010), Zipfel et al. (2011) and Baratoux et al. (2011). Except for the last paper, the original lander/rover and spacecraft data are only K; Th was derived from K/Th for TES surface type 1 and 2 ratios from Taylor et al. (2008) as applicable; for the last paper, the original Th data were converted with K/Th = 5510 (Taylor et al., 2006, major volcanic provinces). The line K/Th = 5530 (Taylor et al., 2006, global crust) and the WD and LF compositions (checkered diamonds) are included for reference.

Table 4
Approximate present-day average surface and total crustal concentrations of ^{40}K and Th in ppb by weight inferred from observations.

Model	^{40}K	Th
Meteorites (averages of bulk compositions)[a]		
Basaltic shergottites	19–295	44–730
Olivine-phyric shergottites	16–180	11–409
Lherzolitic shergottites[b]	18–117	27–150
Nakhlites (clinopyroxenites)[c]	105–495	150–850
Chassignites (dunites)	49–54	51–130
Orthopyroxenites	18	62
Lander/rover measurements (Pathfinder, Spirit, Opportunity; averages)[a]		
Northern plains, rock[d]	68–913	126–1696
Northern plains, soils[d]	379–571	704–1070
Spacecraft measurements (averages)[a]		
Northern plains	452	710
Southern highlands	425	700
various S highland provinces	220–379[e]	360–620
various low-albedo provinces	97	166[f]
Global crust (Phobos 2[g])	207–413	1900–3100
Global crust (Mars Odyssey GRS[h])	340–410	620–700

[a] ^{40}K calculated from total K for a present-day fraction of 1.17×10^{-4} (Jaupart and Mareschal, 2003).
[b] Upper limit of Th (NWA6342) estimated with K/Th = 6660.
[c] Upper limit of K (NWA5790) estimated with K/Th = 6004.
[d] Th inferred from K/Th = 4600 (TES surface type 2) (Taylor et al., 2008).
[e] Baratoux et al. (2011); from K/Th = 5220 for ancient southern highlands (Taylor et al., 2006).
[f] Poulet et al. (2009); from K/Th = 5000 for low-albedo data (TES surface type 1) from Mars Express, Observatoire pour la Minéralogie, l'Eau, les Glaces et l'Activité (OMEGA) (Taylor et al., 2006).
[g] Trombka et al. (1991), probably biased toward southern highlands and Tharsis volcanics.
[h] Taylor et al. (2006), Taylor and McLennan (2009) and Hahn and McLennan (2010).

K concentrations are available, but Th and U are also given in many cases; gaps in the analytical data were filled by calculating K/Th from reliable complete K–Th datasets for meteorites from the same class. The meteorites fall into several different petrological categories, but all seem to be of crustal origin, in some cases probably representing some sort of mafic or ultramafic cumulate (e.g., Meyer, 2006; McSween, 2008). They are likely to cover a considerable depth range, but their exact geographical and hence geological provenances are not known, and as a consequence of their generally young age of a few hundred million years to ~1.4 Gy, they may overrepresent late-stage volcanic material rather than average crust. K and Th concentrations in meteorites overlap to some extent with the other data types but are in general substantially lower, consistent with derivation from a more depleted mantle than average crust.

Our models give crustal concentrations that are several times lower than rover and spacecraft data but lie well within the field defined by the meteorites, with the exception of the clinopyroxenites (nakhlites), which are richer in K and Th. The models also show an enrichment relative to the initial composition (WD in most cases) approximately along the K/Th ratio line of the global crustal mean from Taylor et al. (2006) (Fig. 10); as this figure shows, the LF concentration model and the two corresponding model data points from model LC-LF, which lie next to the LF symbol, do not match the independent data well. It is reassuring that our melting model is consistent with the meteorite compositions, but most results lie within a narrow range, which makes it difficult to discern better models from worse ones on the basis of compositions. Given the rover and spacecraft data, a stronger crustal enrichment may seem desirable, and the enriched models LC-Tpotl and LC-dTc0, which lie higher up the K/Th = 5330 line, show a potential avenue for coming closer to this goal; somewhat higher crustal radionuclide concentrations may also improve the match of the heat flow results. On the other hand, the discrepancy between meteorite concentrations and rover and spacecraft data raises the question whether the surface concentrations represented by the latter are truly representative for the entire crust; a detailed analysis of gamma-ray spectrometer (GRS) data from Mars Odyssey indicates that the methods that probe only the surface may see compositions affected by hydrological processes or other reactions specific to near-surface environments that lead to an enrichment of K and Th at the surface (Newsom et al., 2007). As such processes are not included in our models, meteorite concentrations and our results may represent mean crustal compositions as resulting from mantle melting better than the rover and spacecraft data suggest. Furthermore, the analysis of meteorites indicates that the martian mantle is chemically heterogeneous and that at least some of the heterogeneities have been very long-lived and may be related to ancient primary crust (e.g., Taylor and McLennan, 2009). As we started after the period of primary crust formation and assumed an initially homogeneous mantle, our models cannot be expected to reproduce such characteristics; they are, however, consistent with an already depleted mantle, which has also been inferred as being the source of shergottites (e.g., Taylor and McLennan, 2009), which are products of late volcanism. In that case, the WD radionuclide contents should be regarded as representative of already depleted mantle and cannot be used to determine the original bulk silicate concentrations by simply calculating how much has decayed since ~4.5 Ga.

4.4. Crustal thickness and magnetization

Crustal thickness is controlled by the integrated history of melt generation, which is strongest in the first 1–1.5 Gy. In a discrete numerical model, in which "crust" is formally described as material with a negative melting degree f beyond a certain threshold value, the crustal thickness can in principle vary with the choice of this value, and the accuracy with which it can be determined is limited by the resolution of the numerical grid. However, the transition from crust to mantle is very sharp, so that crustal thicknesses can be determined with a better resolution than the grid by linear interpolation between the two grid points bracketing the crust–mantle boundary and vary only by a few kilometers for all reasonable choices of the threshold value.

All of our models except the LF and the Tpotl pairs and the nomlt pair, which does not produce any crust by definition, generate a crust with a final average thickness between 77 and 97 km, and most show thickness variations with an amplitude of 20–25 km. The average thicknesses for the LF pair lie between 130 and 140 km as a consequence of the higher mantle temperature, whereas the cool mantle of the Tpotl pair yields a thickness of only 43 (LC) and 60 km (SC). All these values lie within independent estimates of the mean thickness of the crust from gravity and magnetic data, which range from ~30 to 150 km but generally give preference to values less than 100 km (Nimmo and Stevenson, 2001; Neumann et al., 2004; Wieczorek and Zuber, 2004. see Table 5). The detailed model of Neumann et al. (2004) suggests a mean value of 45 km, but their crustal thickness histogram shows two maxima representing the northern lowlands and the southern highlands. The average thickness in the latter region is likely near the peak at ~57 km in that histogram, and crustal thickness can be estimated to vary by 20–25 km around that value, similar to the variation in our models. Both our thickness and the growth evolution also compare well with the parameterized models by Schumacher and Breuer (2006) and Breuer and Spohn (2006), most of which yield a final thickness between ~40 and 110 km, depending on thermal conductivity, mantle temperature, and the presence of an initial crust (Fig. 11). As those studies as well as our own models show, the time at which crust formation drops to very low rates depends on a variety of factors, e.g., initial temperature and initial crustal thickness. Observations suggest that most of the crust was formed in the Noachian (e.g., Werner, 2009), and a subset of the aforementioned models supports the possibility that crust formation began to decline strongly by 3.7–3.5 Ga, indicating that most of our models overpredict the duration of large-scale crust formation and that crust formation may have been more intense in the first billion years of martian evolution. This mismatch is in part a consequence of the unavoidably artificial initial condition we used and of the omission of processes in the first 500 My. The results from Hauck and Phillips (2002) and Breuer and Spohn (2006) and the evolution of model LC-Tpotl (Fig. 11) suggest that the initial temperature and the primordial crustal thickness are crucial parameters that can lead to a closer agreement for models that start at 4.4–4.5 Ga. On the other hand, when considering the timing, it should be kept in mind that the ratio of extrusive to intrusive crustal formation or the importance of underplating may have evolved on Mars, and such changes would be more difficult to detect with dating methods that rely on crater size–frequency distributions and might shift the cessation of crustal formation to a more recent time.

When comparing observation-based estimates, which often give a global average that is affected by the crustal dichotomy, with those from our models, we have to distinguish between purely magmatic crustal formation and a crust that has also been shaped markedly by a giant impact (e.g., Marinova et al., 2008). In the first

Table 5
Crustal thickness in km at 4 Gy from models and inferred from observations. Mantle depths in the different series are: LC, 1700 km; MC, 1825 km; SC, 1950 km.

Model	Model feature	$h_{\mathrm{c,ave}}$	$h_{\mathrm{c,min}}$
Models of this study			
LC-ref	Reference case	79	55
LC-LF	Tripled ^{40}K	131	91
LC-Mg80	Mg# = 0.8	77	52
LC-Tpotl	$T_{\mathrm{pot}} = 1773$ K	43	31
LC-WNc	Different core α, c_p, k (cf. Table 2)	79	61
LC-dTc0	No superheated core	79	59
LC-mx1	Melt extraction above 1%	77	58
LC-mx2	Melt extraction above 2%	86	62
LC-nolat	Latent heat of phase transitions = 0	85	59
LC-v0	Surface porosity 0%	78	57
LC-v50	Surface porosity 50%	76	57
LC-dcht	Crustal dichotomy	74	43
MC-Tpotm/v35	$T_{\mathrm{pot}} = 1843$ K, surface porosity 35%	80	53
SC-ref	Reference case	85	59
SC-LF	Tripled ^{40}K	136[a]	–
SC-Mg80	Mg# = 0.8	82	55
SC-Tpotl	$T_{\mathrm{pot}} = 1773$ K	60	39
SC-WNc	Different core $\alpha,\ c_p,\ k$ (cf. Table 2)	84	60
SC-dTc0	No superheated core	97	68
SC-mx1	Melt extraction above 1%	80	59
SC-mx2	Melt extraction above 2%	90	69
SC-nolat	Latent heat of phase transitions = 0	91	58
SC-v0	Surface porosity 0%	83	55
SC-v50	Surface porosity 50%	89	67
SC-dcht	Crustal dichotomy	79	50
Other studies			
Breuer and Spohn (2006), standard model		110	
Cheung and King (2011), southern highlands		~90–100	
Konopliv et al. (2006)		72	
Neumann et al. (2004), global		> 45	< 15
Neumann et al. (2004), southern highlands		58	
Nimmo and Stevenson (2001)		30–100	
Ruiz et al. (2008)		45–65	
Schumacher and Breuer (2006)		67–102	
Turcotte et al. (2002)		90	
Wieczorek and Zuber (2004)		50	38

[a] Estimated value.

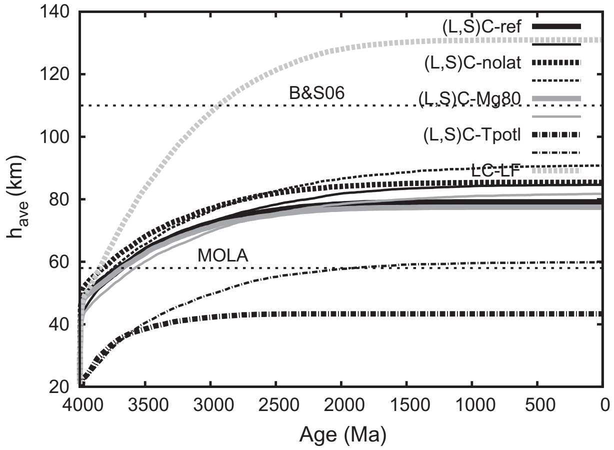

Fig. 11. Average crustal thickness as a function of time for the reference models, the nolat, Mg80, and Tpotl pairs, and model LC-LF (large core: thick lines; small core: thin lines). Also shown are the lower bound on the mean crustal thickness of the southern highlands inferred from altimetry and gravity measured by the Mars Orbiter Laser Altimeter (MOLA, Neumann et al., 2004) and the upper bound from Breuer and Spohn (2006), labeled B&S06.

case, the highland–lowland dichotomy could be interpreted as the contrast between one domain with enhanced and one with diminished melt production or as the expression of an almost hemisphere-sized region of low melt productivity within a fertile reference mantle. Such an endogenic scenario corresponds to the situation in our models, but the models do not reproduce the observed bimodal thickness distribution. If the highlands crust corresponds to crust produced by reference mantle, its thickness is best suited for comparison with our models; otherwise the global average is appropriate. By contrast, the second case, i.e., the giant impact scenario, involves an exogenic factor not included in our models that causes a redistribution of crust and partial loss of former crustal material and whose effects prevail even after billions of years (e.g., Golabek et al., 2011). For comparison with most of our models, the thickness of the highland crust reduced by the average thickness of the ejecta deposits, which is likely on the order of a few kilometers (also see Appendix C), is probably the best choice. Whatever the cause of the dichotomy, the fact that the imposed dichotomy in the dcht model pair has a final difference in thickness between the two domains of only ~15 km in spite of the much larger initial contrast suggests that the mantle beneath the thin-crust domain has a strongly reduced fertility in order to maintain the large observed thickness contrast over billions of years.

In all pairs, the SC model produces a crust that is thicker by 3–18 km on average than that of its LC counterpart, because the temperature of the mantle decreases more slowly in SC models than in LC models. Apart from this, the potential temperature is the most important controlling factor with regard to crustal thickness. The absence of the latent heat effects of phase transitions in the mantle in the nolat pair enhances crust production by a few percent. Other factors such as the threshold of melt retention or the initial core superheat also lead to variations of a few kilometers and cannot be constrained better with available data, given the large range of independent values. The Mg# of the mantle and the thermoelastic properties of the core do not have any notable impact on crust production.

The decreasing fraction of growing crust suggests that volcanic activity becomes more and more concentrated in certain areas that are related to plumes, the tops of which would be among the last parts of the upper mantle to cool below the solidus. In order to assess a possible connection between thermal anomalies at the CMB and crustal thickness, we calculate a cumulative thermal anomaly distribution defined by

$$\Delta T_{\mathrm{cum}}(\phi, z, t) = \frac{1}{t}\int_0^t (T(\phi, z, t') - T_{\mathrm{ave}}(z, t'))\mathrm{d}t' \tag{14}$$

at each point (ϕ, z) for a depth z near the CMB, where $T_{\mathrm{ave}}(z)$ is the horizontally averaged temperature at that depth at time t. This quantity is a measure of the thermal history of a given point at depth z. For instance, regions that have been affected by plumes for a major part of the planet's history would appear as maxima, and in case of a connection with crustal thickness, the immobile crust would tend to be thicker above such a region. The correlation coefficient between $\Delta T_{\mathrm{cum}}(\phi, z)$ and crustal thickness $h_{\mathrm{c}}(\phi, z)$ reaches maximum values between ~ 0.25 and ~ 0.6. The LC models generally reach the highest correlation values between 1 and 2.5 Gy and decline substantially afterwards, when crust production also ceases; this transition occurs when plume tops cool below the solidus temperature. By contrast, many of the SC models, in which deep-mantle temperatures remain a bit higher and melt production persists longer, do not show such a clear decline. These results concerning crust production suggest that continuation of volcanic activity up to the present would be more consistent with a small core and would be focused at plume-generated hotspots. The analysis of the geological record, especially crater retention ages, confirms that most of the crust was formed in the Noachian and Hesperian. However, the presence of relatively scarcely cratered volcanic flows as well as the young ages of martian meteorites indicate that some volcanic activity must have persisted up to more recent times, possibly to the present (e.g., Hartmann and Neukum, 2001; Werner, 2009), but that this activity is likely concentrated around Tharsis and Elysium (e.g., Robbins et al., 2011; Hauber et al., 2011).

The greatest unknown in this context is probably the variation of melt productivity with supersolidus temperature, which is unconstrained for $p \gtrsim 2$ GPa. If our assumption is correct that f changes as rapidly over tens of degrees above the solidus in the garnet stability field as it does in the spinel lherzolite field, then the precise form of that function is probably of minor importance. However, if the productivity rises less steeply with T, then we would overpredict crustal thickness and growth rate. The generally good agreement between our models and independent results suggests that our melting model is fairly robust, but this question can be answered only by new experimental constraints.

The thickness of the magnetized crust can be derived from our models. We find that the depth to the Curie temperature often increases with time by a factor of 3–4 but is nonetheless generally near the crustal thickness or even larger in the earliest stages of the models. For the magnetic part of the crust, Voorhies (2008) and Ravat (2011) found a typical thickness of 48 and 40 km, respectively, from the analysis of orbital magnetometer data, and Nimmo and Gilmore (2001) deduced a depth to the Curie temperature of ~35 km from the demagnetization at impact craters. Ruiz et al. (2006a) placed the Curie temperature at the time of magnetization between 35 and 54 km depth, depending on the amount of crustal radionuclides and the dominant magnetic carrier mineral. Arkani-Hamed (2005) found depths to Curie temperatures for magnetite and hematite of ~85 and ~100 km at the time of magnetization. The lower values can be accommodated by all models except the Tpotl pair, in which the crustal thickness remains below 30 km for the first ~150 My; at least if the magnetic carrier mineral is magnetite or hematite, we do not expect a substantially different outcome even if we had included crustal heating by intrusive magmatism. The higher values seem rather unlikely in the context of our models, because they would require either a much quicker growth of the crust or the survival of the dynamo well into the

Amazonian. If we accept the lower values of the depth to the Curie temperature and assume that most or all of the Noachian crust was magnetized, we can use those estimates to judge our models not by the final but by the starting crustal thickness that developed from the initial conditions. Except for the Tpotl pair, they fall within the range of values suggested by the depth to the Curie temperature or slightly exceed its upper bound (Figs. 11 and 12). The temporal evolution curves can also be extrapolated linearly backwards in time to 4.5 Ga, under the assumption of an approximately linear increase of crustal thickness with time as suggested by many parameterized evolution models (e.g., Breuer and Spohn, 2006; Schumacher and Breuer, 2006), in order to estimate the thickness of the very earliest crust. Of the models in Fig. 11, models LC-ref and LC-Mg80 (as well as the nolat pair) would yield values around 30 km at 4.5 Ga, whereas SC-ref and SC-Mg80 as well as LC-LF would have a mean thickness between 10 and 20 km and the Tpotl models would start with no crust at all. These figures suggest that the thickness estimates from Norman (1999, 2002) could be matched with a slightly lower initial temperature than in the reference case, but the uncertainties associated with such an extrapolation as well as with the parameterized models are magnified by the fact that they neglect the influence of multiple impacts on melting and crust formation.

4.5. Mantle properties

The thermal and petrological changes of the mantle during planetary evolution also cause other secular changes, e.g., in the average mantle density, which slowly increases, usually by 5–15 kg/m^3 after 4 Gy; only the hottest models (LF and nomlt) show an intermediate decrease by 10–20 kg/m^3 during the first half of the modeled time span. The density of the core is estimated to increase by 35–100 kg/m^3. Our algorithm does not allow actual contraction of the numerical grid, but under the assumption that mass is conserved, the calculated change in density can be used to estimate a decrease in radius of the whole planet of 12–17 km for most LC models and of 3–4 km for most SC models. The latter range brackets closely the upper limit of $\sim$3.8 km for the radius decrease since the Early Noachian ($\gtrsim$ 4 Ga) derived by Nahm and Schultz (2011) from the study of contractional features on the martian surface. Similar to the model proposed by those authors, the highest rate of change falls in the first $\sim$200 My, although the later decrease is not as uniform in our models.

The viscosity profiles at 4 Gy resemble in range and shape those of Steinberger et al. (2010). The most important difference from their models is that the lithosphere in our models is thicker; the reason may partly lie in the fact that they calculated the viscosity using a temperature profile with an upper thermal boundary layer whose thickness is derived from a gravity-based estimate of the elastic lithospheric thickness. Furthermore, these authors did not find a viscosity increase in the basal layer of the small-core model, probably because of the effect of their imposed thermal boundary layer at the CMB. The position of the phase transition in their model is slightly more compatible with that in our reference case with Mg# = 0.75 than with the Mg80 models, but the viscosity displays a small decrease instead of an increase in their models, which may be due to an elevated water content; this possibility is explored in Ruedas et al. (submitted for publication).

4.6. Areoid and moment of inertia

Our predicted heights of the reference gravitational equipotential surface, or areoid, show some variation but lie mostly between approximately -200 and 200 m in large-core and -300 and 300 m in small-core models. Because most of our models lack the crustal dichotomy, we consider only extremal values here and compare them with the extrema of the MGGM08A isostatic geoid (corrected for a linear relation between gravity and topography) of -332 and 639 m (Marty et al., 2009). The closest match is achieved by the small-core reference model (-326 m/620 m), and the extrema of models LC-Mg80 and LC-v50 also fall within 150 m of the observed value. They also display a particularly strong dominance of the spectral component of harmonic degree 2, as does model LC-dcht (Fig. 13). Many of the models reproduce the dominance of harmonic degree 2 and the general trend given by Kaula's law, but as this figure reveals, even the best models show some substantial differences from observations at harmonic degrees as low as 4 to 6.

The inclusion of a parameterized core model allows us to estimate the normalized moment of inertia (MoI)

$$I = \frac{8\pi}{3MR^2}\int_0^R \bar{\varrho}(r)r^4\,\mathrm{d}r \tag{15}$$

for our models, where we have neglected the flattening of the planet and $\bar{\varrho}(r)$ is the horizontally averaged density. All present-day values lie between approximately 0.3598 and 0.3681, and most fall between 0.3646 and 0.3666 (LC models) and 0.3636 and 0.3652 (SC models and MC-Tpotm/v35). The best estimate for the mean moment of inertia of Mars lies between 0.36432 and 0.36538 (Konopliv et al., 2011). Hence, many small-core models, including the SC reference model, give a close match, and models SC-Tpotl and SC-v0 as well as MC-Tpotm/v35 lie within that bracket; so do models LC-LF and LC-v50, whereas most of the other large-core models yield a bit higher values. The match of several LC models in this respect could be improved by reducing the size of the core by a few tens of kilometers or increasing Mg# by 0.01 or 0.02, or both. The MoI of Mars would be a bit different if the planet did not have a crustal dichotomy, but the effect is expected to be smaller than the observational error; this point is discussed in detail in Appendix C.

5. Conclusions

We have developed a method to integrate information about thermodynamic properties of planetary materials into a geodynamic mantle convection algorithm, applied it to modeling of the thermal and compositional evolution of Mars over the past 4 Gy, and derived predictions for comparison with a range of quantities that are observed or inferred from observations. Most of our mod-

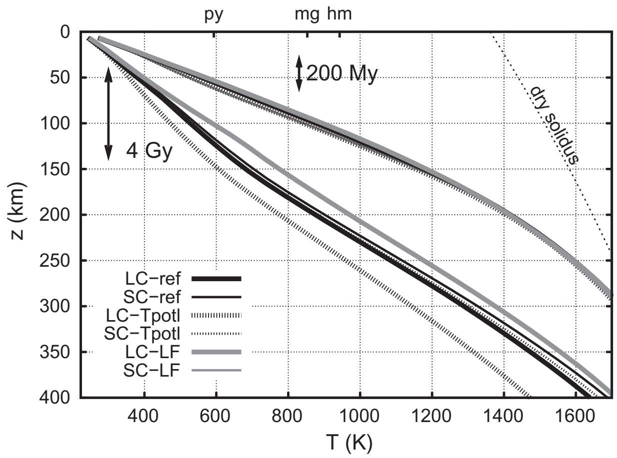

Fig. 12. Laterally averaged temperature in the uppermost mantle at 200 My and 4 Gy for selected models representing the full range of areotherms of all melt-producing models. The double-headed arrows indicate the range of crustal thicknesses of all plotted models at 200 My and 4 Gy, respectively. The Curie temperatures for hematite (hm), magnetite (mg), and pyrrhotite (py) are also marked.

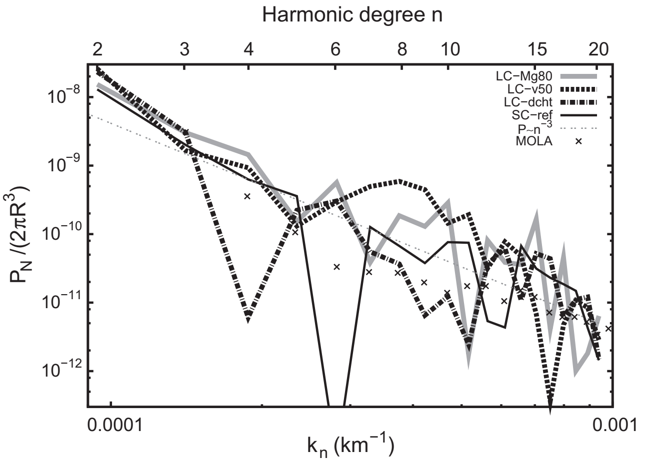

Fig. 13. Normalized power spectral density of the areoid P_N as a function of wavenumber $k_n = n/(2\pi R)$ and harmonic degree n for the four best models up to $n = 20$ at 4 Gy; also plotted for comparison are the coefficients from MOLA observations and the relation $P_N \sim 1/k_n^{-3}$ known as Kaula's law (Turcotte et al., 2002).

els can account for some subset of these quantities reasonably well, although none matches all of them, indicating that some features of Mars stem from ancient perturbations and have not been modified substantially since then. Still, some conclusions can be drawn about the martian interior and about the sensitivity of geophysical and geochemical observables to certain properties of the planet.

Large-core models tend to match most observations better than small-core models, but no single model is a clear favorite. In particular, it appears difficult to sustain a core dynamo in small-core models even for short periods, and they generally also perform worse in reproducing features of the areoid. On the other hand, small-core models may explain better the secular thermal contraction of the planet; however, this is one property that in principle cannot be modeled accurately with our means and should therefore not be valued too highly. The final verdict on the question of core size may come from the Seismic Experiment for Interior Structure (SEIS, e.g., Mimoun et al., 2012) and the Rotation and Interior Structure Experiment (RISE, e.g., Van Hoolst et al., 2012) on the InSight mission in 2016, as they are expected to give direct seismic information about the depth to the CMB and improve markedly the accuracy of MoI determinations. Fixing the former parameter will remove the need to consider large-core and small-core cases in modeling studies such as ours. A detailed and self-consistent rock-physical framework can then be used as input for seismic modeling as has been carried out for Earth (e.g., Goes et al., 2004; Styles et al., 2011; Nakagawa et al., 2012). An important reason for the contrast between large-core and small-core models lies in the presence at the base of the mantle in the latter models of a perovskite+ferropericlase layer, which exerts a substantial control on mantle and core dynamics and evolution. The mid-mantle phase transitions are dynamically of much lesser importance, and convection encompasses the entire mantle; only a basal pv + fp layer, if present, would be less involved.

On the basis of large-core model results, we estimate that the potential temperature of the mantle at the end of the Noachian was ~1840 K and that the temperature step across the CMB was close to zero; hence, the initial temperature excess of the core at the CMB may have been 100–150 K. Lithospheric heat flux results are quite similar for all models, so that this is not a strong discriminant. The thickness of the magnetized crust is not a strong criterion to judge models either, but the results suggest that hematite or magnetite are more likely to be the magnetic carrier mineral than pyrrhotite.

Although plumes form in most models and become fewer during the evolution of the planet, it is difficult to produce a stable pattern of two or three stationary plumes in the mantle early under our model assumptions; the size of the core is not decisive, although small-core models tend to result in fewer plumes. This general outcome suggests that the conditions for the formation of such a pattern, if it has been present in the martian mantle, are set very early in the planet's history and are connected to heterogeneities in the mantle and/or boundary conditions (e.g., van Thienen et al., 2006; Zhong, 2009). A model pair that includes a crustal dichotomy has not revealed a strong effect of this feature, however. That our omission of that early stage and the simplifying assumptions concerning the initial conditions do not lead to such a pattern at a later stage suggests that martian mantle evolution can be divided into two strongly different stages, of which the second, i.e., the ~4 Gy since the end of the late heavy bombardment on which this study focuses, does not involve sufficiently vigorous convection to produce structures on a global scale and obliterate the heritage of the first few hundred million years. In order to explain long-lasting volcanism in Tharsis and Elysium, scenarios with a succession of shorter-lived plumes rising from limited CMB regions should be explored as an alternative to the traditional long-lived superplumes.

Bulk silicate Mg# and radionuclide concentrations in line with those suggested by Wänke and Dreibus (1994) are more likely to reflect the composition of the martian mantle than those suggested by Lodders and Fegley (1997) or a markedly less iron-rich composition. If InSight delivers high-quality seismic data, it may be possible to carry out further geochemical modeling with seismically determined positions of phase boundaries and compare the results with our models. However, a homogeneous initial condition such as that adopted here fails to reproduce the heterogeneity observed in martian crustal samples, so a more enriched mantle source is likely to exist; hence, our models support conclusions on this point drawn from geochemical studies of martian meteorites. Our calculated crustal concentrations are consistent with meteorite data but do not come near the concentrations measured by rovers and spacecraft at the surface. Whereas we probably underestimate crustal concentrations, the comparison with the meteorites suggests that those surface concentrations may involve processes other than igneous fractionation and may not be representative of the entire crust.

The effects of mantle water, particularly regarding the uncertainty in the radial viscosity structure of the mantle, are important to several aspects of convection and melting and are investigated in a companion paper (Ruedas et al., submitted for publication). One of the results of the present study, namely that none of our models reproduces well the inferred viscosity profile of Mars by Steinberger et al. (2010), will be of special interest with respect to these effects.

Acknowledgments

We are grateful for the constructive comments of Steven Hauck and the editor, Mark Jellinek, on this manuscript and for those of Doris Breuer and Tilman Spohn on an earlier version of it. We also appreciate helpful discussions with Yingwei Fei, who also kindly provided the data for the solidus parameterized by Eq. 11, and we thank Paul Asimow, Anne Hofmeister, David Kohlstedt, Konstantin Litasov, Michelle Minitti, Angèle Ricolleau, Steven Shirey, Jessica Warren, and Li Zhang for advice. Bernhard Steinberger generously made available a copy of his paper prior to publication. The research reported in this paper has mostly been supported by the NASA Planetary Geology and Geophysics Program through grants NNG04GI64G and NNX07AP50G. Resources supporting this work were provided by the NASA High-End Computing (HEC) Program through the NASA Center for Climate Simulation (NCCS) at Goddard Space Flight Center, awards SMD-09-1310 and SMD-10-1816.

Appendix A. Supplementary data

Supplementary data associated with this article can be found, in the online version, at http://dx.doi.org/10.1016/j.pepi.2012.12.002.

Appendix B. Implementation of the core

The core provides the thermal boundary condition at the bottom of the mantle convection model, and its own thermal evolution is in turn influenced by the mantle. The heat flux across the CMB is important for the dynamical processes in the mantle and is also linked to the existence of a dynamo. In order to capture the characteristics of the evolution of the core essential to the mantle model, we adapted and modified the model of Nimmo et al. (2004). This adaptation and some departures from the original procedure made in our algorithm are described in this appendix.

B.1. Simplified phase diagram

Contrary to the Earth's core, the martian core is expected to be substantially richer in sulfur, and the pressure to which the material of the core is subjected is much lower. As a consequence, the iron polymorph to be used as a reference is not hcp iron but fcc iron. The phase diagram in the Fe–S system is complicated by the presence of a eutectic whose position in p, T space varies with sulfur content. From its dependence on pressure (Li and Fei, 2003; Stewart et al., 2007; Chen et al., 2008; Kamada et al., 2010), the weight fraction of sulfur at the eutectic can be described in a simplified form as

$$X_{\mathrm{eu}} = 0.189994 \exp(-0.0855032p) + 0.123914 \tag{B.1a}$$

and its temperature as

$$T_{\mathrm{eu}} = 15.7388p + 928.283 + 332.323 \exp(-0.145753p). \tag{B.1b}$$

For the liquidi of the pure end-members, experimental data (Li and Fei, 2003; Urakawa et al., 2004; Boehler and Ross, 2007) yield

$$T_{\mathrm{m,Fe}}(p) = 1811(1.01437p^{0.994887} - 0.985349p + 1) \tag{B.1c}$$

$$T_{\mathrm{m,FeS}}(p) = 1478(0.237718p^{0.975156} - 0.203506p + 1). \tag{B.1d}$$

After conversion of mass fraction X to mole fraction $\underline{X}$, it is possible to parameterize the melting temperature of the core alloy in $(p, T, \underline{X}_{\mathrm{S}})$ below ~ 50 GPa:

$$T_{\mathrm{m}}(p, \underline{X}_{\mathrm{S}}) = \begin{cases} T_{\mathrm{m,Fe}}(p) + \frac{T_{\mathrm{eu}} - T_{\mathrm{m,Fe}}(p)}{\ln(1-\underline{X}_{\mathrm{eu}})} \ln(1 - \underline{X}_{\mathrm{S}}) & \underline{X}_{\mathrm{S}} \leqslant \underline{X}_{\mathrm{eu}} \\ T_{\mathrm{m,FeS}}(p) + \frac{T_{\mathrm{eu}} - T_{\mathrm{m,FeS}}(p)}{\ln\left(\frac{1}{2} + \underline{X}_{\mathrm{eu}}\right)} \ln\left(\frac{1}{2} + \underline{X}_{\mathrm{S}}\right) & \text{else;} \end{cases} \tag{B.1e}$$

p is given in GPa and T in K in all equations. The second summands account for the liquidus depression caused by addition of $\underline{X}_{\mathrm{S}}$ mol% of a minor component, whereby the theoretical terms $1 + \ln(1 - \underline{X}_{\mathrm{S}})$ and $\ln\left(\frac{1}{2} + \underline{X}_{\mathrm{S}}\right)$ (after Stevenson, 1981; Anderson, 1998) are scaled with an empirical factor to match the available experimental constraints.

B.2. Thermoelastic properties and core adiabat

Following Labrosse et al. (2001), Nimmo et al. (2004) parameterized the density and the adiabat as functions of the radius:

$$\varrho(r) = \varrho_{\mathrm{cen}} \exp\left(-\frac{r^2}{L^2}\right) \tag{B.2}$$

$$T(r) = T_{\mathrm{cen}} \exp\left(-\frac{r^2}{D^2}\right), \tag{B.3}$$

where the scaling lengths L and D are given by

$$L = \sqrt{\frac{3K_{S0}\left[\ln\left(\frac{\varrho_{\mathrm{cen}}}{\varrho_0}\right) + 1\right]}{2\pi G \varrho_0 \varrho_{\mathrm{cen}}}} \quad \text{and} \tag{B.4}$$

$$D = \sqrt{\frac{3c_p}{2\pi G \alpha_{\mathrm{c}} \varrho_{\mathrm{cen}}}}. \tag{B.5}$$

Here, G is the gravitational constant, α_{c} and c_p are the thermal expansion coefficient and the specific heat of the core alloy and are assumed to be constant, and the subscripts 0 and cen indicate values at a reference pressure and at the center of the planet, respectively. It is worth noting that due to the fact that Eq. B.4 is derived from the second-order logarithmic equation of state, which is not accurate over large pressure ranges, values different from those at surface pressure have to be used; this is why those authors had to choose K_{S0}, ϱ_0, and ϱ_{cen} so that L approximates the PREM density profile even though the material parameters do not correspond to a state occupied by the material. We determined the density profile of the mantle first as described in the main text and thus know the mass of the core beforehand. Together with the chosen core radius, the resulting average density of the core can be used together with the K_{S0} and ϱ_0 determined for reference conditions near the martian CMB to solve Eqs. B.2 and B.4 iteratively for ϱ_{cen} and L. The $\varrho(r)$ profile given by Eq. B.2 is thus consistent with the density profiles for the mantle that result from the convection model in the sense that it reproduces the average density of the core.

In this simple model α_{c} and c_p – or indeed the ratio c_p/α_{c} – are constant through the pressure range of the core. An average α_{c} is determined with Eq. 8 for the sulfur content corresponding to the core size of the model from the liquid iron, fcc iron and solid FeS V end-member values from Anderson and Isaak (2000), Boehler (2000), Komabayashi and Fei (2010) and Urakawa et al. (2004), from which we also took ϱ_0 and K_{T0} for the calculation of K_{S0}; for c_p, the value of 780 J/(kg K) (Williams and Nimmo, 2004) was used. As we did not find a usable dataset for a Fe–S liquid, we determined the actual parameters needed for the model, in which the core is liquid, by rescaling the solid alloy parameters using their counterparts for liquid and solid pure iron. Lacking a martian equivalent to PREM, we can only compare the density profiles calculated in this way with the (solid) density profiles from Bertka and Fei (1998) and find that they approximate them reasonably closely given the uncertainties in temperature and the difference in the assumed state. The density profiles can also be used to compute the planet's moment of inertia, given radial symmetry.

B.3. Entropy and thermal conductivity

In agreement with Williams and Nimmo (2004) we found that the martian core has been molten throughout the past 4 Gy, so that the contributions from latent heat release due to core crystallization and solution of S and from gravitational energy to the core's energy balance are zero. Likewise, the contribution from molecular diffusion is at least two orders of magnitude smaller than the other terms and can thus be neglected. The total entropy available to drive a dynamo hence includes contributions from the specific heat of the core, S_s, from the decay of radionuclides, S_R, and from conductive heat transport along the adiabat, S_k:

$$S_{\mathrm{tot}} = S_s + S_R - S_k \tag{B.6}$$

(cf. Williams and Nimmo, 2004); for the explicit form of S_s, S_R, and S_k, the reader is referred to the paper by Nimmo et al. (2004). One major uncertainty here is related to S_R and to the solubility of radionuclides in the core alloy. Recent work by Corgne et al. (2007) indicated that the metal–silicate partition coefficient of potassium shows no clear dependence from p, T, or sulfur content but increases with oxygen content in the alloy. Experimental results on oxygen solubility in the iron alloy (Rubie et al., 2004; Tsuno et al., 2011) indicate that the oxygen content of the martian core does not exceed a few percent, which suggests that the concentration of K is only a few tens of ppm, so we adopted a partitioning coefficient of 0.05, which lies in the middle of the range suggested by Corgne et al. (2007). Uranium is even more incompatible ($D_\mathrm{U} \approx 0.003$, Malavergne et al., 2007) and is unimportant for radioactive heating of the core; the same is probably true for thorium, for which we assumed $D_\mathrm{Th} = 0$. With these partitioning coefficients, we determined the initial radionuclide contents for the core from those of the mantle. Radiogenic heating therefore is much smaller in our models than in some of those by Williams and Nimmo (2004).

Another uncertainty is introduced by S_k, which is negative because the heat conducted along the adiabat is not available to drive the dynamo. This uncertainty is caused by the poor knowledge of the thermal conductivity of the core alloy k. In a metallic core, the potentially relevant contributions to k stem from electrons and phonons. Following Stacey and Anderson (2001), the electronic contribution was derived from electrical conductivity measurements at low pressures, extrapolated to core conditions and converted to the thermal conductivity by the Wiedemann–Franz law:

$$k_\mathrm{e,l} = L_0 T_\mathrm{m0} \sigma_0 \left(\frac{V}{V_0}\right)^{\frac{1}{3}} \exp\left\{\frac{2\gamma_0}{q}\left[1-\left(\frac{V}{V_0}\right)^q\right]\right\}, \tag{B.7}$$

where $L_0 = 2.44 \cdot 10^{-8}$ W/(S K) is the Lorenz number and σ_0 is the electrical conductivity at the alloy's melting point T_m0 at surface pressure. It is worth noting that contrary to the electrical conductivity, the thermal conductivity of the liquid shows no explicit dependence from T. According to Allgaier (1969), the values of σ_0 of the end-member compositions Fe and FeS differ by about one order of magnitude, and σ_0 varies with S content. Yoshino et al. (2004) carried out bulk electrical conductivity measurements on peridotite–metal assemblages on a eutectic Fe–S composition; we used their values measured at 1273 K for assemblages with 0 and 26 vol% metal, solved the relation for the upper Hashin–Shtrikman bound for the metal conductivity, and derived a value of ~59100 S/m for the eutectic Fe–S composition at surface pressure. Together with the range of data from Allgaier (1969), we approximated the compositional dependence as $\sigma_0 = 9.1 \cdot 10^5 \exp(-5.5\underline{X}_\mathrm{S})$ S/m.

Although for crystalline solids the phononic contribution $k_\mathrm{ph,l}$ could be calculated from the classical Debye model, there is apparently no well-established theory for liquids that could be applied easily. By comparing measured electrical and thermal conductivities of liquid iron at surface pressure, Stacey and Anderson (2001) estimated that the lattice conductivity of liquid core material is ~3 W/(m K). As liquids can be seen as structurally similar to amorphous solids such as glasses with zero shear-wave velocity, we used a simple model originally developed as a lower bound on $k_\mathrm{ph,l}$ for amorphous solids (e.g., Cahill et al., 1992) to estimate the "lattice" conductivity. From the material parameters of the molten alloy, we find that the phononic contribution is on the order of 1 W/(m K), i.e., comparable to the estimate of Stacey and Anderson (2001) and much smaller than the electronic contribution. Depending on the size of the core and the corresponding S content, we find a total average thermal conductivity $k_\mathrm{l} = k_\mathrm{e,l} + k_\mathrm{ph,l}$ between ~20 W/(m K) for a small, iron-rich core and less than 10 W/(m K) for a pure FeS core, i.e., it is substantially lower than assumed by Williams and Nimmo (2004), even without including the correction for certain changes in the electronic structure at high pressures suggested by Stacey and Loper (2007). This result is consistent with the electrical conductivity data from Allgaier (1969), which indicate that liquid FeS is a rather poor conductor.

Appendix C. MoI of a spherical equivalent of Mars

The figure of Mars departs from an ideal sphere as a consequence of rotational deformation, but also because of the crustal dichotomy that manifests itself as a global-scale topographical contrast between the northern and the southern hemisphere. By contrast, our models are for a spherical planet. In this appendix we estimate the effect on the moment of inertia of mass additions to Mars that would make the planet more similar to our model geometry in order to ensure a meaningful comparison between our calculated MoI and the observed mean MoI of Mars.

The angle θ_l between the axis of rotation and the boundary between highlands and lowlands, which is assumed circular and centered on the pole for our purposes, can be calculated from the normalized area of the spherical cap corresponding to the lowlands, $\mathcal{A}_\mathrm{l}$, by

$$\theta_\mathrm{l} = \arccos(1 - 2\mathcal{A}_\mathrm{l}); \tag{C.1}$$

with $\mathcal{A}_\mathrm{l} = 0.42$ (Andrews-Hanna et al., 2008), we have $\theta_\mathrm{l} = 80.8^\circ$. The mass of a cap-like partial spherical shell of uniform density ϱ_c, outer radius R_o and inner radius R_i is

$$\begin{aligned} M &= 2\pi\varrho_\mathrm{c}\int_{R_\mathrm{i}}^{R_\mathrm{o}}\int_0^{\theta_\mathrm{l}} r^2 \sin\theta \,\mathrm{d}r\mathrm{d}\theta \\ &= \frac{2\pi\varrho_\mathrm{c}}{3}\left(R_\mathrm{o}^3 - R_\mathrm{i}^3\right)(1-\cos\theta_\mathrm{l}), \end{aligned} \tag{C.2}$$

and its moment of inertia for rotation about its axis of symmetry is

$$\begin{aligned} I &= 2\pi\varrho_\mathrm{c}\int_{R_\mathrm{i}}^{R_\mathrm{o}}\int_0^{\theta_\mathrm{l}} r^4 \sin^3\theta \,\mathrm{d}r\mathrm{d}\theta \\ &= \frac{2\pi\varrho_\mathrm{c}}{15}\left(R_\mathrm{o}^5 - R_\mathrm{i}^5\right)\left(2 - 3\cos\theta_\mathrm{l} + \cos^3\theta_\mathrm{l}\right). \end{aligned} \tag{C.3}$$

For comparison with a spherical model, the non-spherical figure of Mars has to be replaced by a suitable equivalent sphere of constant crustal thickness, which involves the removal of the surface topography associated with the crustal dichotomy and the equalization of the topography of the crust–mantle boundary. A hypsogram of martian topography relative to the center of mass and for a radius R_ref of 3396 km as a reference for determining the shape of the planet indicates that, on average, the northern lowlands lie $\Delta R_\mathrm{l} \approx 3$ km below the zero level and the southern highlands $\Delta R_\mathrm{h} \approx 1.5$ km above it (Smith et al., 1999; Aharonson et al., 2001). The most recent determination of the normalized polar MoI, $C/(MR_\mathrm{ref}^2)$, yielded a value between 0.3644 and 0.3652, from which follows a mean MoI, $I/(MR^2)$, between 0.36432 and 0.36538 after correcting for the effect of Tharsis' topography on the MoI, which is not included in our models (Konopliv et al., 2011). Many studies of martian shape, MoI, and gravity include a crustal density ϱ_c of 2900 kg/m^3 and a mantle density of ϱ_m of 3500 kg/m^3 (e.g., Neumann et al., 2004). The topographical difference between highlands and lowlands, $\Delta R_\mathrm{h} + \Delta R_\mathrm{l}$, is mirrored by a difference of

$$z_\mathrm{h} - z_\mathrm{l} = \Delta z_\mathrm{hl} = \frac{\varrho_\mathrm{c}}{\varrho_\mathrm{m} - \varrho_\mathrm{c}}(\Delta R_\mathrm{h} + \Delta R_\mathrm{l}) \tag{C.4}$$

in the depth of the crust–mantle boundary between the two domains, under the assumption of isostatic equilibrium and an Airy-type crust model. With the values for ϱ_c and ϱ_m given above, Eq. C.4 yields 21.75 km. This figure is the thickness of the uppermost mantle beneath the lowlands that has to be replaced by crustal material in a balancing calculation.

We consider two cases and test each of them with a thin crust (~47 km average thickness, similar to Neumann et al., 2004) and a thick crust (90 km average thickness, Turcotte et al., 2002, similar to the upper bound of our models). In the first case, we fill the lowlands to the level of the highlands by adding a basalt layer of thickness $\Delta R_\mathrm{h} + \Delta R_\mathrm{l}$ and replacing upper mantle with crustal material as described above, so that the crust has a globally uniform thickness corresponding to that of the highlands. Depending on the original mean MoI, the resulting reduced MoI is 0.3640 or 0.3651 after rescaling to a sphere of radius R that corresponds to our models; differences caused by the different crustal thicknesses are smaller than 10^{-4} and hence smaller than the observational errors given by Konopliv et al. (2011). This case may apply if the highlands are regarded as ancient, volcanic crust that was formed by partial melting of fertile mantle, whereas the thinner crust of the lowlands is the product of melting that was reduced in magnitude for some reason.

In the second case, we fill the lowlands only to R_ref, which corresponds to zero elevation (Smith et al., 1999), by adding a basalt layer of thickness ΔR_l, and remove the highlands by deleting a basalt layer of thickness ΔR_h; the mantle beneath the lowlands is treated in the same way as before so that the crust is now thinner by ΔR_h than in the first case. The resulting reduced MoI is 0.3641 or 0.3651, i.e., the same as before within errors. This case may apply, for instance, if zero elevation represents a topographical mean, the highlands a region of excess crust formation, and the lowlands of diminished crust formation. Alternatively, the lowlands may have been excavated by an impact, and a part of the ejecta may have deposited on the highlands, as suggested by several studies (e.g., Marinova et al., 2008, 2011). In the most likely scenario of these impact models, ~25% of the melt generated by the impact are deposited outside the impact cavity (i.e., in the highlands) and ~10% are lost from the planet; the rest remains inside the cavity, most of it at the surface, and the fraction of evaporated material is negligible. The volume "missing" between the zero elevation level and the surface of the lowlands, i.e., the ejecta, thus corresponds to ~35% of the melt generated by the impact, and ~71% of that missing mass should now be present as deposits in the highlands. Indeed, the volume of highland crust above zero elevation differs by only 2.6% from the expected ejecta layer volume.

References

Aharonson, O., Zuber, M.T., Rothman, D.H., 2001. Statistics of Mars' topography from the Mars Orbiter Laser Altimeter: slopes, correlations, and physical models. J. Geophys. Res. 106, 23723–23735.

Allgaier, R.S., 1969. Interpretation of transport measurements in electronically conducting liquids. Phys. Rev. 185, 227–244.

Anderson, O.L., 1998. The Grüneisen parameter for iron at outer core conditions and the resulting conductive heat and power in the core. Phys. Earth Planet. Inter. 109, 179–197.

Anderson, O.L., Isaak, D.G., 2000. Calculated melting curves for phases of iron. Am. Mineral. 85, 376–385.

Andrews-Hanna, J.C., Zuber, M.T., Banerdt, W.B., 2008. The Borealis basin and the origin of the martian crustal dichotomy. Nature 453, 1212–1215.

Arkani-Hamed, J., 2005. Magnetic crust of Mars. J. Geophys. Res. 110, E08005. http://dx.doi.org/10.1029/2004JE002397.

Auzende, A.-L., Badro, J., Ryerson, F.J., Weber, P.K., Fallon, S.J., Addad, A., Siebert, J., Fiquet, G., 2008. Element partitioning between magnesium silicate perovskite and ferropericlase: New insights into bulk lower-mantle geochemistry. Earth Planet. Sci. Lett. 269, 164–174.

Banerdt, W.B., Smrekar, S., Alkalai, L., Hoffman, T., Warwick, R., Hurst, K., Folkner, W., Lognonné, P., Spohn, T., Asmar, S., Banfield, D., Boschi, L., Christensen, U., Dehant, V., Giardini, D., Goetz, W., Golombek, M., Grott, M., Hudson, T., Johnson, C., Kargl, G., Kobayashi, N., Maki, J., Mimoun, D., Mocquet, A., Morgan, P., Panning, M., Pike, W.T., Tromp, J., van Zoest, T., Weber, R., Wieczorek, M.InSight Team, 2012. InSight: An Integrated Exploration of the Interior of Mars. Lunar Planet. Sci. XLIII (Abstract 2838).

Baratoux, D., Toplis, M.J., Monnereau, M., Gasnault, O., 2011. Thermal history of Mars inferred from orbital geochemistry of volcanic provinces. Nature 472, 338–341 (correction in 475, p.254).

BasuSarbadhikari, A., Day, J.M.D., Liu, Y., Rumble III, D., Taylor, L.A., 2009. Petrogenesis of olivine-phyric shergottite Larkman Nunatak 06319: implications for enriched components in martian basalts. Geochim. Cosmochim. Acta 73, 2190–2214.

Berryman, J.G., 1995. Mixture theories for rock properties. In: Ahrens, T.J. (Ed.), Rock Physics & Phase Relations — A Handbook of Physical Constants, AGU Reference Shelf, 3. American Geophysical Union, Washington, DC, pp. 205–228.

Bertka, C.M., Fei, Y., 1997. Mineralogy of the Martian interior up to core–mantle boundary pressures. J. Geophys. Res. 102, 5251–5264.

Bertka, C.M., Fei, Y., 1998. Density profile of an SNC model Martian interior and the moment-of-inertia factor of Mars. Earth Planet. Sci. Lett. 157, 79–88.

Bertka, C.M., Holloway, J.R., 1994. Anhydrous partial melting of an iron-rich mantle I: subsolidus phase assemblages and partial melting phase relations at 10 to 30 kbar. Contrib. Mineral. Petrol. 115, 313–322.

Blundy, J., Wood, B., 2003. Mineral – melt partitioning of uranium, thorium and their daughters. In: Bourdon, B., Henderson, G.M., Lundstrom, C.C., Turner, S.P. (Eds.), Uranium-series Geochemistry, No. 52 in Rev. Mineral. Geochem.. Mineralogical Society of America, Washington, DC, pp. 59–123.

Boehler, R., 2000. High-pressure experiments and the phase diagram of lower mantle and core materials. Rev. Geophys. 38, 221–245.

Boehler, R., Ross, M., 2007. Properties of rocks and minerals – high-pressure melting. In: Price, G.D. (Ed.), Mineral Physics, Treatise on Geophysics, vol. 2. Elsevier, pp. 527–541.

Boynton, W.V., Taylor, G.J., Karunatillake, S., Reedy, R.C., Keller, J.M., 2008. Elemental abundances determined via the Mars Odyssey GRS. In: Bell, J.F., III (Ed.), The Martian Surface: Composition, Mineralogy, and Physical Properties. Cambridge University Press, pp. 105–124.

Brandon, A.D., Walker, R.J., Morgan, J.W., Gates, G.G., 2000. Re–Os isotopic evidence for early differentiation of the martian mantle. Geochim. Cosmochim. Acta 64, 4083–4095.

Breuer, D., Spohn, T., 2003. Early plate tectonics versus single-plate tectonics on Mars: evidence from magnetic field history and crust evolution. J. Geophys. Res. 108, 5072. http://dx.doi.org/10.1029/2002JE001999.

Breuer, D., Spohn, T., 2006. Viscosity of the Martian mantle and its initial temperature: constraints from crust formation history and the evolution of the magnetic field. Planet. Space Sci. 54, 153–169.

Breuer, D., Yuen, D.A., Spohn, T., 1997. Phase transitions in the Martian mantle: implications for partially layered convection. Earth Planet. Sci. Lett. 148, 457–469.

Bridges, J.C., Warren, P.H., 2006. The SNC meteorites: basaltic igneous processes on Mars. J. Geol. Soc. 163, 229–251.

Cahill, D.G., Watson, S.K., Pohl, R.O., 1992. Lower limit to the thermal conductivity of disordered crystals. Phys. Rev. B 46, 6131–6140.

Chen, B., Li, J., Hauck II, S.A., 2008. Non-ideal liquidus curve in the Fe–S system and Mercury's snowing core. Geophys. Res. Lett. 35, L07201. http://dx.doi.org/10.1029/2008GL033311.

Chennaoui Aoudjehane, H., Avice, G., Barrat, J.-A., Boudouma, O., Chen, G., Duke, M.J.M., Franchi, I.A., Gattacceca, J., Grady, M.M., Greenwood, R.C., Herd, C.D.K., Hewins, R., Jambon, A., Marty, B., Rochette, P., Smith, C.L., Sautter, V., Verchovsky, A., Weber, P., Zanda, B., 2012. Tissint martian meteorite: a fresh look at the interior surface and atmosphere of Mars. Science 338, 785–788.

Cheung, K.K., King, S.D., 2011. Using crustal thickness modeling to study Mars' crustal/mantle structures. Lunar Planet. Sci. XLII. Abstract 1534.

Christensen, U.R., Yuen, D.A., 1985. Layered convection induced by phase transitions. J. Geophys. Res. 90, 10291–10300.

Clifford, S.M., 1993. A model for the hydrologic and climatic behavior of water on Mars. J. Geophys. Res. 98, 10973–11016.

Corgne, A., Keshav, S., Fei, Y., McDonough, W.F., 2007. How much potassium is in the Earth's core? New insights from partitioning experiments. Earth Planet. Sci. Lett. 256, 567–576.

Courtial, P., Ohtani, E., Dingwell, D.B., 1997. High-temperature densities of some mantle melts. Geochim. Cosmochim. Acta 61, 3111–3119.

Debaille, V., Brandon, A.D., O'Neill, C., Yin, Q.-Z., Jacobsen, B., 2009. Early martian mantle overturn inferred from isotopic composition of nakhlite meteorites. Nat. Geosci. 2, 548–552.

Draper, D.S., Xirouchakis, D., Agee, C.B., 2003. Trace element partitioning between garnet and chondritic melt from 5 to 9 GPa: implications for the onset of the majorite transition in the martian mantle. Earth Planet. Sci. Lett. 139, 149–169.

Elkins-Tanton, L.T., Parmentier, E.M., Hess, P.C., 2003. Magma ocean fractional crystallization and cumulate overturn in terrestrial planets: implications for Mars. Meteorit. Planet. Sci. 38, 1753–1771.

Elkins-Tanton, L.T., Zaranek, S.E., Parmentier, E.M., Hess, P.C., 2005. Early magnetic field and magmatic activity on Mars from magma ocean cumulate overturn. Earth Planet. Sci. Lett. 236, 1–12.

Faul, U.H., 2001. Melt retention and segregation beneath mid-ocean ridges. Nature 410, 920–923.

Fei, Y., Van Orman, J., Li, J., van Westrenen, W., Sanloup, C., Minarik, W., Hirose, K., Komabayashi, T., Walter, M.J., Funakoshi, K.-I., 2004. Experimentally determined postspinel transformation boundary in Mg_2SiO_4 using MgO as an internal pressure standard and its geophysical implications. J. Geophys. Res. 109, B02305. http://dx.doi.org/10.1029/2003JB002562.

Filiberto, J., Chin, E., Day, J.M.D., Franchi, I.A., Greenwood, R.C., Gross, J., Penniston-Dorland, S.C., Schwenzer, S.P., Treiman, A.H., 2012. Geochemistry of intermediate olivine-phyric shergottite Northwest Africa 6234, with similarities to basaltic shergottite Northwest Africa 480 and olivine-phyric shergottite Northwest Africa 2990. Meteorit. Planet. Sci. 47, 1256–1273.

Filiberto, J., Dasgupta, R., 2011. Fe^{2+}–Mg partitioning between olivine and basaltic melts: Applications to genesis of olivine-phyric shergottites and conditions of melting in the Martian interior. Earth Planet. Sci. Lett. 304, 527–537.

Filiberto, J., Dasgupta, R., Kiefer, W.S., Treiman, A.H., 2010. High pressure, near-liquidus phase equilibria of the Home Plate basalt Fastball and melting in the martian mantle. Geophys. Res. Lett. 37, L13201. http://dx.doi.org/10.1029/2010GL043999.

Foley, C.N., Economou, T., Clayton, R.N., 2003. Final chemical results from the Mars Pathfinder alpha proton X-ray spectrometer. J. Geophys. Res. 108, 8096. http://dx.doi.org/10.1029/2002JE002019.

Forsyth, D.W., Scheirer, D.S., Webb, S.C., Dorman, L.M., Orcutt, J.A., Harding, A.J., Blackman, D.K., Phipps Morgan, J., Detrick, R.S., Shen, Y., Wolfe, C.J., Canales, J.P., Toomey, D.R., Sheehan, A.F., Solomon, S.C., Wilcock, W.S.D., 1998. Imaging the deep seismic structure beneath a mid-ocean ridge: the MELT experiment. Science 280, 1215–1218.

Gasparik, T., 2003. Phase Diagrams for Geoscientists. Springer, Berlin.

Goes, S., Cammarano, F., Hansen, U., 2004. Synthetic seismic signature of thermal mantle plumes. Earth Planet. Sci. Lett. 218, 403–419.

Golabek, G.J., Keller, T., Gerya, T.V., Zhu, G., Tackley, P.J., Connolly, J.A.D., 2011. Origin of the martian dichotomy and Tharsis from a giant impact causing massive magmatism. Icarus 215, 346–357.

Grott, M., Hauber, E., Werner, S.C., Kronberg, P., Neukum, G., 2005. High heat flux on ancient Mars: evidence from rift flank uplift at Coracis Fossae. Geophys. Res. Lett. 32, L21201. http://dx.doi.org/10.1029/2005GL023894.

Grott, M., Hauber, E., Werner, S.C., Kronberg, P., Neukum, G., 2007. Mechanical modeling of thrust faults in the Thaumasia region, Mars, and implications for the Noachian heat flux. Icarus 186, 517–526.

Hahn, B.C., McLennan, S.M., 2010. Regional martian crustal heat flow from Mars Odyssey gamma-ray spectrometry. Lunar Planet. Sci. XLI. Abstract 1371.

Hansen, U., Yuen, D.A., Kroening, S.E., Larsen, T.B., 1993. Dynamical consequences of depth-dependent thermal expansivity and viscosity on mantle circulations and thermal structure. Phys. Earth Planet. Int. 77, 201–223.

Harder, H., 1998. Phase transitions and the three-dimensional planform of thermal convection in the Martian mantle. J. Geophys. Res. 103, 16775–16798.

Harder, H., Christensen, U.R., 1996. A one-plume model of martian mantle convection. Nature 380, 507–509.

Harlow, G.E., 1997. K in clinopyroxene a high pressure and temperature: an experimental study. Am. Mineral. 82, 259–269.

Hartmann, W.K., Neukum, G., 2001. Cratering chronology and the evolution of Mars. Space Sci. Rev. 96, 165–194.

Hauber, E., Brož, P., Jagert, F., Jodłowski, P., Platz, T., 2011. Very recent and wide-spread basaltic volcanism on Mars. Geophys. Res. Lett. 38, L10201. http://dx.doi.org/10.1029/2011GL047310.

Hauck, S.A., Phillips, R.J., 2002. Thermal and crustal evolution of Mars. J. Geophys. Res. 107, 5052. http://dx.doi.org/10.1029/2001JE001801.

Hauri, E.H., Wagner, T.P., Grove, T.L., 1994. Experimental and natural partitioning of Th, U, Pb and other trace elements between garnet, clinopyroxene and basaltic melts. Chem. Geol. 117, 149–166.

Head, J.W., Wilson, L., 1992. Magma reservoirs and neutral buoyancy zones on Venus: implications for the formation and evolution of volcanic landforms. J. Geophys. Res. 97, 3877–3903.

Hernlund, J.W., Tackley, P.J., 2007. Some dynamical consequences of partial melting in Earth's deep mantle. Phys. Earth Planet. Int. 162, 149–163.

Hernlund, J.W., Tackley, P.J., 2008. Modeling mantle convection in the spherical annulus. Phys. Earth Planet. Int. 171, 48–54.

Hirth, G., Kohlstedt, D.L., 2003. Rheology of the upper mantle and the mantle wedge: a view from the experimentalists. In: Eiler, J. (Ed.), Inside the Subduction Factory, AGU Geophysical Monograph, 138. American Geophysical Union, Washington, DC, pp. 83–105.

Hofmeister, A.M., 1999. Mantle values of thermal conductivity and the geotherm from phonon lifetimes. Science 283, 1699–1706.

Hofmeister, A.M., Branlund, J.M., Pertermann, M., 2007. Properties of rocks and minerals – thermal conductivity of the Earth. In: Price, G.D. (Ed.), Mineral Physics, Treatise on Geophysics, vol. 2. Elsevier, pp. 543–577.

Hui, H., Peslier, A.H., Lapen, T.J., Shafer, J.T., Brandon, A.D., Irving, A.J., 2011. Petrogenesis of basaltic shergottite Northwest Africa 5298: closed-system crystallization of an oxidized mafic melt. Meteorit. Planet. Sci. 46, 1313–1328.

Ikeda, Y., 2004. Petrology of the Yamato 980459 shergottite. Antarct. Meteorite Res. 17, 35–54.

Imae, N., Ikeda, Y., 2007. Petrology of the Miller Range 03346 nakhlite in comparison with the Yamato-000593 nakhlite. Meteorit. Planet. Sci. 42, 171–184.

Irving, A.J., Bunch, T.E., Kuehner, S.M., Herd, C.D.K., Gellissen, M., Lapen, T.J., Rumble III, D., Pitt, D., 2011. Petrologic, elemental and isotopic characterization of shock-melted, enriched ultramafic poikilitic shergottite Northwest Africa 6342. Lunar Planet. Sci. XLII, 1612.

Irving, A.J., Kuehner, S.M., Herd, C.D.K., Gellissen, M., Korotev, R.L., Puchtel, I., Walker, R.J., Lapen, T.J., Rumble III, D., 2010a. Petrologic, elemental and multi-isotopic characterization of permafic olivine-phyric shergottite Northwest Africa 5789: A primitive magma derived from depleted martian mantle. Lunar Planet. Sci. XLI. Abstract 1547.

Irving, A.J., Kuehner, S.M., Herd, C.D.K., Gellissen, M., Rumble III, D., 2010b. Olivine-bearing diabasic shergottite Northwest Africa 5990: Petrology and composition of a new type of depleted martian igneous rock. Lunar Planet. Sci. XLI. Abstract 1833.

Ita, J., Stixrude, L., 1992. Petrology, elasticity, and composition of the mantle transition zone. J. Geophys. Res. 97, 6849–6866.

Ito, E., Takahashi, E., 1989. Postspinel transformations in the system $Mg_2SiO_4 - -Fe_2SiO_4$ and some geophysical implications. J. Geophys. Res. 94, 10637–10646.

Jaupart, C., Mareschal, J.-C., 2003. Constraints on crustal heat production from heat flow data. In: Rudnick, R.L. (Ed.), The Crust, vol. 3, Treatise on Geochemistry, Elsevier. pp. 65–84.

Jin, Z.-M., Zhang, J., Green II, H.W., Jin, S., 2001. Eclogite rheology: Implications for subducted lithosphere. Geology 29, 667–670.

Jing, Z., Karato, S.-i., 2009. The density of volatile bearing melts in the Earth's deep mantle: the role of chemical composition. Chem. Geol. 262, 100–107.

Jones, J.H., 1995. Experimental trace element partitioning. In: Ahrens, T.J. (Ed.), Rock Physics and Phase Relations – A Handbook of Physical Constants, vol. 3, AGU Reference Shelf, American Geophysical Union, Washington, DC. pp. 73–104.

Kamada, S., Terasaki, H., Ohtani, E., Sakai, T., Kikegawa, T., Ohishi, Y., Hirao, N., Sata, N., Kondo, T., 2010. Phase relationships of the Fe–FeS system in conditions up to the Earth's outer core. Earth Planet. Sci. Lett. 294, 94–100.

Katsura, T., Ito, E., 1989. The system $Mg_2SiO4–Fe_2SiO_4$ at high pressures and temperatures: precise determination of stabilities of olivine, modified spinel, and spinel. J. Geophys. Res. 94, 15663–15670.

Katsura, T., Yamada, H., Nishikawa, O., Song, M., Kubo, A., Shinmei, T., Yokoshi, S., Aizawa, Y., Yoshino, T., Walter, M.J., Ito, E., Funakoshi, K.-i. 2004. Olivine–wadsleyite transition in the system $(Mg,Fe)_2SiO_4$. J. Geophys. Res. 109, B02209. http://dx.doi.org/10.1029/2003JB002438.

Katz, R.F., Spiegelman, M., Langmuir, C., 2003. A new parameterization of hydrous mantle melting. Geochem. Geophys. Geosyst. 4, 1073. http://dx.doi.org/10.1029/2002GC000433.

Keller, T., Tackley, P.J., 2009. Towards self-consistent modeling of the martian dichotomy: the influence of one-ridge convection on crustal thickness distribution. Icarus 202, 429–443.

Khan, A., Connolly, J.A.D., 2008. Constraining the composition and thermal state of Mars from inversion of geophysical data. J. Geophys. Res. 113, E07003. http://dx.doi.org/10.1029/2007JE002996.

Kiefer, W.S., 2003. Melting in the martian mantle: shergottite formation and implications for present-day mantle convection on Mars. Meteorit. Planet. Sci. 38, 1815–1832.

Komabayashi, T., Fei, Y., 2010. Internally consistent thermodynamic database for iron to the Earth's core conditions. J. Geophys. Res. 115, B03202. http://dx.doi.org/10.1029/2009JB006442.

Konopliv, A.S., Asmar, S.W., Folkner, W.M., Karatekin, Ö., Nunes, D.C., Smrekar, S.E., Yoder, C.F., Zuber, M.T., 2011. Mars high resolution gravity fields from MRO, Mars seasonal gravity, and other dynamical parameters. Icarus 211, 401–428.

Konopliv, A.S., Yoder, C.S., Standish, E.M., Yuan, D.-N., Sjogren, W.L., 2006. A global solution for the Mars static and seasonal gravity, Mars orientation, Phobos and Deimos masses, and Mars ephemeris. Icarus 182, 32–50.

Kostopoulos, D., James, S.D., 1992. Parameterization of the melting regime of the shallow upper mantle and the effects of variable lithospheric stretching on mantle modal stratification and trace-element concentrations in magmas. J. Petrol. 33, 665–691.

Kronberg, P., Hauber, E., Grott, M., Werner, S.C., Schäfer, T., Gwinner, K., Giese, B., Masson, P., Neukum, G. 2007. Acheron Fossae, Mars: tectonic rifting, volcanism, and implications for lithospheric thickness. J. Geophys. Res. 112, E04005. http://dx.doi.org/10.1029/2006JE002780.

Kubo, T., Ohtani, E., Kondo, T., Kato, T., Toma, M., Hosoya, T., Sano, A., Kikegawa, T., Nagase, T., 2002. Metastable garnet in the oceanic crust at the top of the lower mantle. Nature 420, 803–806.

Kuehner, S.M., Irving, A.J., Herd, C.D.K., Gellissen, M., Lapen, T.J., Rumble III, D., 2011. Pristine olivine-phyric shergottite Northwest Africa 6162: a primitive magma with accumulated crystals derived from depleted martian mantle. Lunar Planet. Sci. XLII. Abstract 1610.

Labrosse, S., Poirier, J.-P., Le Mouël, J.-L., 2001. The age of the inner core. Earth Planet. Sci. Lett. 190, 111–123.

Langmuir, C. H., Klein, E. M., Plank, T., 1992. Petrological systematics of mid-ocean ridge basalts: constraints on melt generation beneath ocean ridges. In: Phipps Morgan, J., Blackman, D. K., Sinton, J. M. (Eds.), Mantle7 Flow and Melt Generation at Mid-Ocean Ridges, Geophysical Monograph 71, American Geophysical Union, Washington, DC. pp. 183–280.

Lee, C.-T.A., Luffi, P., Plank, T., Dalton, H., Leeman, W.P., 2009. Constraints on the depths and temperatures of basaltic magma generation on Earth and other terrestrial planets using new thermobarometers for mafic magmas. Earth Planet. Sci. Lett. 279, 20–33.

Leone, G., Wilson, L., Davies, A.G., 2011. The geothermal gradient of Io: consequences for lithosphere structure and volcanic eruptive activity. Icarus 211, 623–635.

Li, J., Fei, Y., 2003. Experimental constraints on core composition. In: Carlson, R.W. (Ed.), The Mantle and Core, Treatise on Geochemistry, vol. 2. Elsevier, pp. 1–31.

Li, Q., Kiefer, W.S., 2007. Mantle convection and magma production on present-day Mars: effects of temperature-dependent rheology. Geophys. Res. Lett. 34, L16203. http://dx.doi.org/10.1029/2007GL030544.

Lin, Y., Qi, L., Wang, G., Xu, L., 2008. Bulk chemical composition of lherzolitic shergottite Grove Mountains 99027—constraints on the mantle of Mars. Meteorit. Planet. Sci. 43, 1179–1187.

Litasov, K.D., Ohtani, E., 2007. Effect of water on the phase relations in Earth's mantle and deep water cycle. In: Ohtani, E. (Ed.), Advances in High-Pressure Mineralogy, Special Paper 421. Geological Society of America, Boulder, Colorado, pp. 115–146.

Lodders, K., Fegley, Jr., B., 1997. An oxygen isotope model for the composition of Mars. Icarus 126, 373–394.

Mackwell, S.J., Zimmerman, M.E., Kohlstedt, D.L., 1998. High-temperature deformation of dry diabase with application to tectonics on Venus. J. Geophys. Res. 103, 975–984.

Malavergne, V., Tarrida, M., Combes, R., Bureau, H., Jones, J., Schwandt, C., 2007. New high-pressure and high-temperature metal/silicate partitioning of U and Pb: implications for the cores of the Earth and Mars. Geochim. Cosmochim. Acta 71, 2637–2655.

Manga, M., 1996. Mixing of heterogeneities in the mantle: effect of viscosity differences. Geophys. Res. Lett. 23, 403–406.

Marinova, M.M., Aharonson, O., Asphaug, E., 2008. Mega-impact formation of the Mars hemispheric dichotomy. Nature 453, 1216–1219.

Marinova, M.M., Aharonson, O., Asphaug, E., 2011. Geophysical consequences of planetary-scale impacts into a Mars-like planet. Icarus 211, 960–985.

Marty, B., Balmino, G., Duron, J., Rosenblatt, P., Le Maistre, S., Rivoldini, A., Dehant, V., Van Hoolst, T., 2009. Martian gravity field model and its time variations from MGS and Odyssey data. Planet. Space Sci. 57, 350–363.

McGovern, P.J., Solomon, S.C., Smith, D.E., Zuber, M.T., Simons, M., Wieczorek, M.A., Phillips, R.J., Neumann, G.A., Aharonson, O., Head, J.W., 2002. Localized gravity/topography admittance and correlation spectra on Mars: Implications for regional and global evolution. J. Geophys. Res. 107, 5136. http://dx.doi.org/10.1029/2002JE001854, correction in vol. 109, E07007, 10.1029/2004JE002286 (2004).

McSween, H.Y., Wyatt, M.B., Gellert, R., Bell, III, J.F., Morris, R.V., Herkenhoff, K.E., Crumpler, L.S., Milam, K.A., Stockstill, K.R., Tornabene, L.L., Arvidson, R.E., Bartlett, P., Blaney, D., Cabrol, N.A., Christensen, P.R., Clark, B.C., Crisp, J.A., Des Marais, D.J., Economou, T., Farmer, J.D., Farrand, W., Ghosh, A., Golombek, M., Gorevan, S., Greeley, R., Hamilton, V.E., Johnson, J.R., Joliff, B.L., Klingelhöfer, G., Knudson, A.T., McLennan, S., Ming, D., Moersch, J.E., Rieder, R., Ruff, S.W., Schröder, C., de Souza, Jr., P.A., Squyres, S.W., Wänke, H., Wang, A., Yen, A., Zipfel, J., 2006. Characterization and petrologic interpretation of olivine-rich basalts at Gusev Crater, Mars. J. Geophys. Res. 111, E02S10. http://dx.doi.org/10.1029/2005JE002477.

McSween, Jr., H.Y., 2008. Martian meteorites as crustal samples. In: Bell, III, J.F. (Ed.), The Martian Surface: Composition, Mineralogy, and Physical Properties, Cambridge University Press. pp. 383–395.

Meyer, C. 2006. The Mars Meteorite Compendium. Tech. Rep. JSC #27672 Revision C, Astromaterials Research & Exploration Science (ARES)/NASA, Houston. url: <http://curator.jsc.nasa.gov/antmet/mmc/index.cfm>.

Mibe, K., Fujii, T., Yasuda, A., Ono, S., 2006a. Mg–Fe partitioning between olivine and ultramafic melts at high pressures. Geochim. Cosmochim. Acta 70, 757–766.

Mibe, K., Orihashi, Y., Nakai, S., Fujii, T. 2006b. Element partitioning between transition-zone minerals and ultramafic melt under hydrous conditions. Geophys. Res. Lett. 33, L16307. http://dx.doi.org/10.1029/2006GL026999.

Michel, N., Forni, O., 2011. Mars mantle convection: influence of phase transitions with core cooling. Planet. Space Sci. 59, 741–748.

Mimoun, D., Lognonné, P., Banerdt, W.B., Hurst, K., Deraucourt, S., Gagnepain-Beyneix, J., Pike, T., Calcutt, S., Bierwirth, M., Roll, R., Zweifel, P., Mance, D., Robert, O., Nébut, T., Tillier, S., Gabsi, T., Laudet, P., Kerjean, L., Perez, R., Giardini, D., Christensen, U., Garcia, R.; the SEIS Team, 2012. The InSight SEIS experiment. Lunar Planet. Sci. XLIII (Abstract 1493).

Monteux, J., Jellinek, A.M., Johnson, C.L., 2011. Why might planets and moons have early dynamos? Earth Planet. Sci. Lett. 310, 349–359.

Musselwhite, D.S., Dalton, H.A., Kiefer, W.S., Treiman, A.H., 2006. Experimental petrology of the basaltic shergottite Yamato-980459: implications for the thermal structure of the Martian mantle. Meteorit. Planet. Sci. 41, 1271–1290.

Nahm, A.L., Schultz, R.A., 2011. Magnitude of global contraction on Mars from analysis of surface faults: implications for martian thermal history. Icarus 211, 389–400.

Nakagawa, T., Tackley, P.J., Deschamps, F., Connolly, J.A.D., 2012. Radial 1-D seismic structures in the deep mantle in mantle convection simulations with self-consistently calculated mineralogy. Geochem. Geophys. Geosyst. 13, Q11002. http://dx.doi.org/10.1029/2012GC004325.

Neukum, G., Basilevsky, A.T., Kneissl, T., Chapman, M.G., van Gasselt, S., Michael, G., Jaumann, R., Hofmann, H., Lanz, J.K., 2010. The geologic evolution of Mars: episodicity of resurfacing events and ages from cratering analysis of image data and correlation with radiometric ages of Martian meteorites. Earth Planet. Sci. Lett. 294, 204–222.

Neumann, G.A., Zuber, M.T., Wieczorek, M.A., McGovern, P.J., Lemoine, F.G., Smith, D.E.,2004. Crustal structure of Mars from gravity and topography. J. Geophys. Res. 109, E08002. http://dx.doi.org/10.1029/2004JE002262.

Newsom, H.E., Crumpler, L.S., Reedy, R.C., Petersen, M.T., Newsom, G.C., Evans, L.G., Taylor, G.J., Keller, J.M., Janes, D.M., Boynton, W.V., Kerry, K.E., Karunatillake, S., 2007. Geochemistry of Martian soil and bedrock in mantled and less mantled terrains with gamma ray data from Mars Odyssey. J. Geophys. Res. 112, E03S12. http://dx.doi.org/10.1029/2006JE002680.

Nimmo, F., Gilmore, M.S., 2001. Constraints on the depth of magnetized crust on Mars from impact craters. J. Geophys. Res. 106, 12315–12323.

Nimmo, F., Price, G.D., Brodholt, J., Gubbins, D., 2004. The influence of potassium on core and geodynamo evolution. Geophys. J. Int. 156, 363–376.

Nimmo, F., Stevenson, D.J., 2000. Influence of early plate tectonics on the thermal evolution and magnetic field of Mars. J. Geophys. Res. 105, 11969–11979.

Nimmo, F., Stevenson, D.J., 2001. Estimates of Martian crustal thickness from viscous relaxation of topography. J. Geophys. Res. 106, 5085–5098.

Norman, M.D., 1999. The composition and thickness of the crust of Mars estimated from rare earth elements and neodymium-isotopic compositions of Martian meteorites. Meteorit. Planet. Sci. 34, 439–449.

Norman, M.D., 2002. Thickness and composition of the martian crust revisited: Implications of an ultradepleted mantle with a Nd isotopic composition like that of QUE94201. Lunar Planet. Sci. XXXIII. Abstract 1175.

Ogawa, M., Yanagisawa, T., 2011. Numerical models of Martian mantle evolution induced by magmatism and solid-state convection beneath stagnant lithosphere. J. Geophys. Res. 116, E08008. http://dx.doi.org/10.1029/2010JE003777.

O'Hara, M.J., Richardson, S.W., Wilson, G., 1971. Garnet-peridotite stability and occurrence in crust and mantle. Contrib. Mineral. Petrol. 32, 48–68.

Ohtani, E., 1984. Generation of komatiite magma and gravitational differentiation in the deep upper mantle. Earth Planet. Sci. Lett. 67, 261–272.

O'Neill, C.J., Lenardic, A., Jellinek, A.M., Kiefer, W.S., 2007. Melt propagation and volcanism in mantle convection simulations, with applications for Martian volcanic and atmospheric evolution. J. Geophys. Res. 112, E07003. http://dx.doi.org/10.1029/2006JE002799.

Pankov, V.L., Ullmann, W., Heinrich, R., Kracke, D., 1998. Thermodynamics of deep geophysical media. Russ. J. Earth Sci. 1, 11–49.

Phillips, R.J., Zuber, M.T., Solomon, S.C., Golombek, M.P., Jakosky, B.M., Banerdt, W.B., Smith, D.E., Williams, R.M.E., Hynes, B.M., Aharonson, O., Hauck II, S.A., 2001. Ancient geodynamics and global-scale hydrology on Mars. Science 291, 2587–2591.

Poulet, F., Mangold, N., Platevoet, B., Bardintzeff, J.-M., Sautter, V., Mustard, J.F., Bibring, J.-P., Pinet, P., Langevin, Y., Gondet, B., Aléon-Toppani, A., 2009. Quantitative compositional analysis of martian mafic regions using the MEx/OMEGA reflectance data: 2. Petrological implications. Icarus 201, 84–101.

Råheim, A., Green, D.H., 1979. Experimental determination of the temperature and pressure dependence of the Fe-Mg partition coefficient for coexisting garnet and clinopyroxene. Contrib. Mineral. Petrol. 48, 179–203.

Ravat, D., 2011. Interpretation of Mars southern highlands high amplitude magnetic field with total gradient and fractal source modeling: new insights into the magnetic mystery of Mars. Icarus 214, 400–412.

Robbins, S.J., Di Achille, G., Hynek, B.M., 2011. The volcanic history of Mars: high-resolution crater-based studies of the calderas of 20 volcanoes. Icarus 211, 1179–1203.

Roberts, J.H., Arkani-Hamed, J., 2012. Impact-induced mantle dynamics on Mars. Icarus 218, 278–289.

Roberts, J.H., Zhong, S., 2006. Degree-1 convection in the Martian mantle and the origin of the hemispheric dichotomy. J. Geophys. Res. 111, E06013. http://dx.doi.org/10.1029/2005JE002668.

Rubie, D.C., Gessmann, C.K., Frost, D.J., 2004. Partitioning of oxygen during core formation on the Earth and Mars. Nature 429, 58–61.

Ruedas, T., 2006. Dynamics, crustal thicknesses, seismic anomalies, and electrical conductivities in dry and hydrous ridge-centered plumes. Phys. Earth Planet. Int. 155, 16–41.

Ruedas, T., Tackley, P.J., 2008. Phase transition evolution and convection style in the martian mantle. Lunar Planet. Sci. XLIX. Abstract 1504.

Ruedas, T., Tackley, P.J., Solomon, S.C., submitted for publication. Thermal and compositional evolution of the martian mantle: effect of water. Phys. Earth Planet. Int.

Ruiz, J., Fernández, C., Gomez-Ortiz, D., Dohm, J.M., López, V., Tejero, R., 2008. Ancient heat flow, crustal thickness, and lithospheric mantle rheology in the Amenthes region, Mars. Earth Planet. Sci. Lett. 270, 1–12.

Ruiz, J., López, V., Dohm, J.M., 2010. The present-day thermal state of Mars. Icarus 207, 631–637.

Ruiz, J., McGovern, P.J., Jiménez-Díaz, A., López, V., Williams, J.-P., Hahn, B.C., Tejero, R., 2011. The thermal evolution of Mars as constrained by paleo-heat flows. Icarus 215, 508–517.

Ruiz, J., McGovern, P.J., Tejero, R., 2006a. The early thermal and magnetic state of the cratered highlands of Mars. Earth Planet. Sci. Lett. 241, 2–10.

Ruiz, J., Tejero, R., McGovern, P.J., 2006b. Evidence for a differentiated crust in Solis Planum, Mars, from lithospheric strength and heat flow. Icarus 180, 308–313.

Ruiz, J., Williams, J.-P., Dohm, J.M., Fernández, C., López, V., 2009. Ancient heat flow and crustal thickness at Warrego rise, Thaumasia highlands, Mars: Implications for a stratified crust. Icarus 203, 47–57.

Sanloup, C., Jambon, A., Gillet, P., 1999. A simple chondritic model of Mars. Phys. Earth Planet. Int. 112, 43–54.

Saxena, S.K., Chatterjee, N., Fei, Y., Shen, G., 1993. Thermodynamic Data on Oxides and Silicates. Springer, Berlin/Heidelberg.

Schmerr, N.C., Fei, Y., Bertka, C., 2001. Extending the solidus for a model iron-rich martian mantle composition to 25 GPa. Lunar Planet. Sci. XXXII. Abstract 1157.

Schmidt, M.E., McCoy, T.J., 2010. The evolution of a heterogeneous Martian mantle: clues from K, P, Ti, Cr, and Ni variations in Gusev basalts and shergottite meteorites. Earth Planet. Sci. Lett. 296, 67–77.

Schott, B., van den Berg, A.P., Yuen, D.A., 2001. Focussed time-dependent martian volcanism from chemical differentiation coupled with variable thermal conductivity. Geophys. Res. Lett. 28, 4271–4274.

Schumacher, S., Breuer, D.,2006. Influence of a variable thermal conductivity on the thermochemical evolution of Mars. J. Geophys. Res. 111, E02006. http://

dx.doi.org/10.1029/2005JE002429 (Correction in vol. 111, E09011, http://dx.doi.org/10.1029/2006JE002755 (2006)).

Schumacher, S., Breuer, D., 2007. An alternative mechanism for recent volcanism on Mars. Geophys. Res. Lett. 34, L14202. http://dx.doi.org/10.1029/2007GL030083.

Schumacher, S., Zegers, T.E., 2011. Aram Chaos and its constraints on the surface heat flux of Mars. Icarus 211, 305–315.

Seyler, M., Toplis, M.J., Lorand, J.-P., Luguet, A., Cannat, M., 2001. Clinopyroxene microtextures reveal incompletely extracted melts in abyssal peridotites. Geology 29, 155–158.

Shaw, D.M., 1970. Trace element fractionation during anatexis. Geochim. Cosmochim. Acta 34, 237–243.

Shirai, N., Ebihara, M., 2004. Chemical characteristics of a Martian meteorite, Yamato 980459. Antarct. Meteorite Res. 17, 55–67.

Smith, D.E., Zuber, M.T., Solomon, S.C., Phillips, R.J., Head, J.W., Garvin, J.B., Banerdt, W.B., Muhleman, D.O., Pettengill, G.H., Neumann, G.A., Lemoine, F.G., Abshire, J.B., Aharonson, O., Brown, C.D., Hauck, S.A., Ivanov, A.B., McGovern, P.J., Zwally, H.J., Duxbury, T.H., 1999. The global topography of Mars and implications for surface evolution. Science, 284, 1495–1503.

Sohl, F., Schubert, G., Spohn, T., 2005. Geophysical constraints on the composition and structure of the Martian interior. J. Geophys. Res. 110, E12008. http://dx.doi.org/10.1029/2005JE002520.

Sohl, F., Spohn, T., 1997. The interior structure of Mars: implications from SNC meteorites. J. Geophys. Res. 102, 1613–1636.

Solomatov, V.S., Stevenson, D.J., 1993. Nonfractional crystallization of a terrestrial magma ocean. J. Geophys. Res. 98, 5391–5406.

Solomon, S.C., 1979. Formation, history and energetics of cores in terrestrial planets. Phys. Earth Planet. Int. 19, 168–182.

Spence, D.A., Ockendon, J.R., Wilmott, P., Turcotte, D.L., Kellogg, L.H., 1988. Convective mixing in the mantle: the role of viscosity differences. Geophys. J. 95, 79–86.

Spohn, T., Grott, M., Knollenberg, J., van Zoest, T., Kargl, G., Smrekar, S.E., Banerdt, W.B., Hudson, T.L.; HP^3 Instrument Team 2012. InSight: Measuring the martian heat flow using the Heat Flow and Physical Properties Package (HP^3). Lunar Planet. Sci. XLIII (Abstract 1445).

Stacey, F.D., Anderson, O.L., 2001. Electrical and thermal conductivities of Fe–Ni–Si alloy under core conditions. Phys. Earth Planet. Int. 124, 153–162.

Stacey, F.D., Loper, D.E., 2007. A revised estimate of the conductivity of iron alloy at high pressure and implications for the core energy balance. Phys. Earth Planet. Int. 161, 13–18.

Steinberger, B., Werner, S.C., Torsvik, T.H., 2010. Deep vs shallow origin of gravity anomalies, topography and volcanism on Earth, Venus and Mars. Icarus 207, 564–577.

Stevenson, D.J., 1981. Models of the Earth's core. Science 214, 611–619.

Stewart, A.J., Schmidt, M.W., van Westrenen, W., Liebske, C., 2007. Mars: A new core-crystallization regime. Science 316, 1323–1325.

Styles, E., Goes, S., van Keken, P.E., Ritsema, J., Smith, H., 2011. Synthetic images of dynamically predicted plumes and comparison with a global tomographic model. Earth Planet. Sci. Lett. 311, 351–363.

Tackley, P.J., 1996. Effects of strongly variable viscosity on three-dimensional compressible convection in planetary mantles. J. Geophys. Res. 101, 3311–3332.

Tackley, P.J., 2008. Modelling compressible mantle convection with large viscosity contrasts in a three-dimensional spherical shell using the yin-yang grid. Phys. Earth Planet. Inter. 171, 7–18.

Tackley, P.J., King, S.D., 2003. Testing the tracer ratio method for modeling active compositional fields in mantle convection simulations. Geochem. Geophys. Geosyst. 4, 8302. http://dx.doi.org/10.1029/2001GC000214.

Taylor, G.J., Boynton, W., Brückner, J., Wänke, H., Dreibus, G., Kerry, K., Keller, J., Reedy, R., Evans, L., Starr, R., Squyres, S., Karunatillake, S., Gasnault, O., Maurice, S., d'Uston, C., Englert, P., Dohm, J., Baker, V., Hamara, D., Janes, D., Sprague, A., Kim, K., Drake, D., 2006. Bulk composition and early differentiation of Mars. J. Geophys. Res. 111, E03S10. http://dx.doi.org/10.1029/2005JE002645.

Taylor, G.J., McLennan, S.M., McSween, Jr., H.Y., Wyatt, M.B., Lentz, R.C.F., 2008. Implications of observed primary lithologies. In: Bell, III, J.F. (Ed.), The Martian Surface: Composition, Mineralogy, and Physical Properties, Cambridge University Press. pp. 501–518.

Taylor, S.R., McLennan, S.M., 2009. Planetary Crusts. Cambridge University Press.

Toplis, M.J., 2005. The thermodynamics of iron and magnesium partitioning between olivine and liquid: criteria for assessing and predicting equilibrium in natural and experimental systems. Contrib. Mineral. Petrol. 149, 22–39.

Treiman, A.H., Irving, A.J., 2008. Petrology of martian meteorite Northwest Africa 998. Meteorit. Planet. Sci. 43, 829–854.

Trombka, J.I., Evans, L.G., Starr, R., Floyd, S.R., Squyres, S.W., Whelan, J.T., Bamford, G.J., Coldwell, R.L., Rester, A.C., Surkov, Y.A., Moskaleva, L.P., Kharyukova, V.P., Manvelyan, O.S., Zaitseva, S.Y., Smirnov, G.G., 1991. Analysis of Phobos mission gamma ray spectra from Mars: Two approaches. Lunar Planet. Sci. XXII, 1415–1416.

Tsuno, K., Frost, D.J., Rubie, D.C., 2011. The effects of nickel and sulphur on the core–mantle partitioning of oxygen in Earth and Mars. Phys. Earth Planet. Int. 185, 1–12.

Turcotte, D.L., Shcherbakov, R., Malamud, B.D., Kucinskas, A.B., 2002. Is the Martian crust also the Martian elastic lithosphere? J. Geophys. Res. 107, 5091. http://dx.doi.org/10.1029/2001JE001594.

Ulmer, P., Stalder, R., 2001. The Mg(Fe)SiO$_3$ orthoenstatite–clinoenstatite transitions at high pressures and temperatures determined by Raman-spectroscopy on quenched samples. Am. Mineral. 86, 1267–1274.

Urakawa, S., Someya, K., Terasaki, H., Katsura, T., Yokoshi, S., Funakoshi, K.-i., Utsumi, W., Katayama, Y., Sueda, Y.-i., Irifune, T., 2004. Phase relationships and equations of state for FeS at high pressures and temperatures and implications for the internal structure of Mars. Phys. Earth Planet. Int., 469–479.

Van Hoolst, T., Dehant, V., Folkner, W., Asmar, S., Rivoldini, A., Banerdt, B., 2012. Interior of Mars from geodesy. Lunar Planet. Sci. XLII. Abstract 2157.

van Keken, P., 2001. Cylindrical scaling for dynamical cooling models of the Earth. Phys. Earth Planet. Int. 124, 119–130.

van Thienen, P., Rivoldini, A., Van Hoolst, T., Lognonné, P., 2006. A top-down origin for martian mantle plumes. Icarus 185, 197–210.

van Thienen, P., Vlaar, N.J., van den Berg, A.P., 2005. Assessment of the cooling capacity of plate tectonics and flood volcanism in the evolution of Earth, Mars and Venus. Phys. Earth Planet. Int. 150, 287–315.

Voorhies, C., 2008. Thickness of the magnetic crust of Mars. J. Geophys. Res. 113, E04004. http://dx.doi.org/10.1029/2007JE002928.

Wadhwa, M., Lentz, R.C.F., McSween, H.Y., Crozaz, G., 2001. A petrologic and trace element study of Dar al Gani 476 and Dar al Gani 489: Twin meteorites with affinities to basaltic and lherzolithic shergottites. Meteorit. Planet. Sci. 36, 195–208.

Walker, D., Agee, C.B., Zhang, Y., 1988. Fusion curve slope and crystal/liquid buoyancy. J. Geophys. Res. 93, 313–323 (correction in vol. 93(B6), 6668).

Wänke, H., Dreibus, G., 1994. Chemistry and accretion history of Mars. Philos. Trans. R. Soc. Lond. A 349, 285–293.

Weinstein, S.A., 1995. The effect of a deep mantle endothermic phase change on the structure of thermal convection in silicate planets. J. Geophys. Res. 100, 11719–11728.

Weisberg, M.K., Smith, C., Benedix, G., Herd, C.D.K., Righter, K., Haack, H., Yamaguchi, A., Chennaoui Aoudjehane, H., Grossman, J.N., 2010. The Meteoritical Bulletin. Meteorit. Planet. Sci. 45 (97), 449–493.

Wenzel, M.J., Manga, M., Jellinek, A.M., 2004. Tharsis as a consequence of Mars' dichotomy and layered mantle. Geophys. Res. Lett. 31, L04702. http://dx.doi.org/10.1029/2003GL019306.

Werner, S.C., 2008. The early martian evolution – constraints from basin formation ages. Icarus 195, 45–60.

Werner, S.C., 2009. The global martian volcanic evolutionary history. Icarus 201, 44–68.

Wieczorek, M.A., Zuber, M.T., 2004. Thickness of the Martian crust: Improved constraints from geoid-to-topography ratios. J. Geophys. Res. 109, E01009. http://dx.doi.org/10.1029/2003JE002153.

Williams, J.-P., Nimmo, F., 2004. Thermal evolution of the Martian core: implications for an early dynamo. Geology 32, 97–100.

Woodland, A.B., Angel, R.J., 2002. Reversal of the orthoferrosilite–high-*P* ferrosilite transition, a phase diagram for FeSiO$_3$, and implications for the mineralogy of the Earth's upper mantle. Eur. J. Mineral. 9, 245–254.

Xie, S., Tackley, P.J., 2004. Evolution of U–Pb and Sm–Nd systems in numerical models of mantle convection and plate tectonics. J. Geophys. Res. 109, B11204. http://dx.doi.org/10.1029/2004JB003176.

Yoshino, T., Walter, M.J., Katsura, T., 2004. Connectivity of molten Fe alloy in peridotite based on in situ electrical conductivity measurements: implications for core formation in terrestrial planets. Earth Planet. Sci. Lett. 222, 625–643.

Yusa, H., Akaogi, M., Ito, E., 1993. Calorimetric study of MgSiO$_3$ garnet and pyroxene: Heat capacities, transition enthalpies, and equilibrium phase relations in MgSiO$_3$ at high pressures and temperatures. J. Geophys. Res. 98, 6453–6460.

Zhao, Y., Zimmerman, M.E., Kohlstedt, D.L., 2009. Effect of iron content on the creep behavior of olivine: 1. Anhydrous conditions. Earth Planet. Sci. Lett. 287, 229–240.

Zhong, S., 2009. Migration of Tharsis volcanism on Mars caused by differential rotation of the lithosphere. Nature Geosci. 2, 19–23.

Zipfel, J., Schröder, C., Jolliff, B.L., Gellert, R., Herkenhoff, K.E., Rieder, R., Anderson, R., Bell, III, J.F., Brückner, J., Crisp, J.A., Christensen, P.R., Clark, B.C., de Souza, Jr., P.A., Dreibus, G., d'Uston, C., Economou, T., Gorevan, S., Hahn, B.C., Klingelhöfer, G., McCoy, T.J., McSween, Jr, H.Y., Ming, D.W., Morris, R.V., Rodionov, D.S., Squyres, S.W., Wänke, H., Wright, S.P., Wyatt, M.B., Yen, A.S., 2011. Bounce Rock—A shergottite-like basalt encountered at Meridiani Planum, Mars. Meteorit. Planet. Sci. 46, 1–20.